Non-Equilibrium Two-State Switching in Mesoscale, Ferromagnetic Particles

A THESIS
SUBMITTED TO THE FACULTY OF THE GRADUATE SCHOOL
OF THE UNIVERSITY OF MINNESOTA
BY

James Thomas Delles

IN PARTIAL FULFILLMENT OF THE REQUIREMENTS
FOR THE DEGREE OF
DOCTOR OF PHILOSOPHY

E. DAN DAHLBERG

July, 2019

Acknowledgements

I would like to extend my sincere gratitude and appreciate to my adviser, Dan, for helping me get this far despite a number of headaches I may have caused him. He kept me focused on the task at hand and because of him, I have become a much better experimentalist. Whenever I got to present to him something that made him happy was something I looked forward to.

None of this would have been accomplished without the help from, and many discussions with, my lab mates: David Harrison, Rob Sponsel, and Barry Costanzi. I would also like to thank my friends outside of the lab who were able to provide me their wisdom when it came to matters of physics and life: Ezra Day-Roberts, John Kohler, and Kevin Sebesta.

My brother and sisters have stood by me and supported me through my entire life and for that, I am truly thankful. My mother was always there for me, probably my biggest fan. My father gave me advise when I was young that I have tried to stick to, "If you are going to do something, you may as well do it right."

And to my wife, Erica, who has been with me through almost all of graduate school. Every problem I have had, she was there to help me bear it. Every happy moment, she was right by my side. I could not have done any of this if she wasn't as supportive as she is.

This work was supported primarily by NSF Grant No. DMR 1609782 and portions were conducted in the Minnesota Nano Center, which is supported by the National Science Foundation through the National Nano Coordinated Infrastructure Network (NNCI) under Award Number ECCS-1542202.

To my wife, Erica.

Abstract

There has been much theoretical study attempting to expand upon the Arrhenius law, $f = f_o exp(U/kT)$, which describes the switching rate in thermally activated, two-state systems, but few experiments to verify it. This is especially true for ferromagnetic particles. Most of the previous experiments performed attempting to study the Arrhenius law focus on the effect the Boltzmann factor, exp(U/kT), has on the switching rate since it dominates any measurement due to its exponential dependence on temperature. This has made it difficult to probe the underlying physics of the prefactor in front of the exponential. Using square, ferromagnetic particles of sizes 250 nm x 250 nm x 10 nm and 210 nm x 210 nm x 10 nm, controlling the barrier height using an applied field, and measuring the average dwell times in each individual state has allowed us to focus on these prefactors. Our measured prefactors vary by twenty five orders of magnitude, and they are smaller than those predicted by previous theories for particles of this size. They become so small as to reach unphysically short timescales. We attribute these unexpectedly small prefactors to our magnetic particles being multidomain and undergoing transitions before the particles have time to reach thermal equilibrium. We show that our particles have a higher probability of transitioning the less time they have been in a state which we attribute to the magnetization spending most of its time near the barrier allowing faster transitions.

Contents

List of Figures

Chapter 1

Introduction

As magnetic systems become smaller, thermal fluctuations become comparable to the sizes of the magnetic energies. When this occurs, the thermal fluctuations can cause the magnetization direction to change stochastically which is an effect known as superparamagnetism. From a technological viewpoint, the magnetization direction fluctuating can be deleterious for something like computer memory where a magnetic bit changing direction can result in corrupted data. For magnetic imaging, it may be beneficial for the magnetization to be able to move freely. These are two examples which highlight the importance of having a reliable system to study this effect to better understand the physics behind it.

A replicatable system allowing us to study thermally activated, switching behavior in one particle at a time with uniform size and shape was developed by Dan Endean.[1] In these particles, their magnetization has two ground states where the particle magnetization points in two different directions. The barrier height separating these two ground states can be controlled by applying an external field which allows us to reduce the barrier height to the order of thermal energies. When the barrier is sufficiently small, thermal fluctuations cause the magnetization direction to fluctuate between the two ground states by transitioning over the barrier. While this is occurring, we used a transport measurement to record the amount of time the magnetization spends in each state individually before switching.

We are able to compare the switching data to an Arrhenius law which allowed us to characterize the switching behavior and attribute it to two parts: an exponential

Boltzmann factor that depends on the barrier height and temperature, and an attempt frequency prefactor which has more complicated physics behind it. This system was then used to probe stochastic resonance by Bern Youngblood[2] and to study the emergence of 1/f noise from a collection of two state oscillators by Barry Costanzi.[3,4]

In the previously cited works, though it was not the topic of their research, they noted that the attempt frequency prefactor varied by many orders of magnitude between samples and also within the same sample at different temperatures and applied fields. What these prefactors had in common was they were larger than expected from the relevant theory for ferromagnetic particles of their size. This unexpected behavior is what prompted the work presented here.

Previous theory work makes certain assumptions that we believe are invalid for our system.[5] The first is that the particle has a uniform magnetization which is not true for a particle of the sizes under study. This resulted in needing to account for these multidomains which are attempting to individually transition over the barrier. The second assumption is that the particle must be in thermal equilibrium before transitioning. We will show that if this assumption is removed, we get the appropriate trend for our theoretical prefactors that is similar to experiment.

Chapter 2 will present the relevant background material for understanding the experiment and results shown. Chapter 3 will explain how the experiment was performed and how the data was interpreted along with a discussion on how magnetic simulations were done. Chapter 4 shows the results of the experiment and simulations with an explanation for the observed behavior. We conclude our findings in Chapter 5 and also propose an experiment that can provide additional verification for the observed behavior.

Chapter 2

Theory and Background

2.1 Magnetostatic Energies and Anisotropies

2.1.1 Exchange Energy and Zeeman Energy

Ferromagnetism arises from the exchange interaction given by

$$E = -2J \sum_{i,j} \boldsymbol{S}_i \cdot \boldsymbol{S}_j, \tag{2.1}$$

where J is the exchange constant and is defined as positive for ferromagnetic systems, i and j are nearest neighbors on the crystalline lattice, and $\boldsymbol{S}$ is the spin of each electron. The exchange energy is minimized when nearest neighbor's spins point in the same direction.

The electron spins also interact with an externally applied, magnetic field, $\boldsymbol{H}$, with the resultant energy known as the Zeeman interaction given by

$$E = -\mu_b \sum_{i} \boldsymbol{S}_i \cdot \boldsymbol{H}, \tag{2.2}$$

where μ_b is the Bohr magneton. The Zeeman energy is minimized when the spins are parallel to the applied field. This can also be expressed in terms of the magnetic moment, $\boldsymbol{\mu}$, of a sample

$$E = -\boldsymbol{\mu} \cdot \boldsymbol{H}, \tag{2.3}$$

where $\boldsymbol{\mu}$ is equal to $\mu_b \sum_i \boldsymbol{S}_i$. If these were the only interactions in the system, the spins would all be parallel with each other and the applied field.

2.1.2 Dipole Energy and Shape Anisotropy

While the exchange and Zeeman interactions minimize the system energy when all the spins are aligned with each other and with the applied field respectively, the dipole interaction may actually increase the system's energy in these circumstances. The dipole interaction energy is given by

$$E = -\frac{\mu_o}{4\pi} \sum_{i,j} \frac{1}{\boldsymbol{r}_{i\to j}^3} [3(\boldsymbol{m}_i \cdot \hat{\boldsymbol{r}}_{i\to j})(\boldsymbol{m}_j \cdot \hat{\boldsymbol{r}}_{i\to j}) - \boldsymbol{m}_i \cdot \boldsymbol{m}_j], \tag{2.4}$$

where μ_o is the vacuum permeability, $\boldsymbol{m_{i,j}}$ are the dipole moments of each spin, and $\hat{\boldsymbol{r}}_{i\to j}$ is the unit vector pointing from one spin to the next. The dipole energy is minimized when spins in a row are parallel, but spins perpendicular to that row are antiparallel. The dipole interaction is much weaker than the exchange interaction but it has a longer range. On short length scales, the exchange interaction dominates and spins want to be parallel, but on longer length scales, the dipole interaction dominates and makes spins want to form magnetic domains of uniform spin direction where the spins between domains are not necessarily aligned.

Another byproduct of the dipole interaction is that spins along the edge of a sample minimize their energy by having their spin be collinear to the edge. This behavior can be compared to a capacitor by analogy where a spin pointing out of the edge is the equivalent of a positive "magnetic" charge and a spin pointing into an edge is a negative "magnetic" charge. If all the spins in the system were parallel, one edge of the sample would have negative charge and the other would have positive charge. This charge distribution in a capacitor would result in a higher system energy and so too does it for the magnetic case. When the spins are collinear to the edge, there are no "magnetic" charges and the dipole energy is reduced.[6] This is known as shape anisotropy since the shape of the sample will have an effect on the magnetic ground state of the system. These dipole fields created by the edges are also known as the demagnetization fields because they result in the measured magnetization being smaller than expected. For highly symmetric samples such as ours under study, there is no shape anisotropy due to the dipole energy being the same in all directions for a uniform magnetization, but the dipole energy still has an effect.

2.1.3 Configurational Anisotropy

Configurational anisotropy arises due to the shape and finite size of a sample. The magnetic spins along the edge of a sample want to be parallel to the edge to minimize their dipole energy. But when the samples are of finite volume, to fully minimuze the dipole energy, the magnetization must curve to be collinear with all the edges and this will increase the exchange energy. It is this balancing between these two energies that makes the configurational anisotropy different from the shape anisotropy since the shape anisotropy depends solely on the dipole energy.[7]

Two samples of the same shape but different size can have ground states that are distinct from one another, but the magnetic states have a tendency to maintain any symmetry of the particle. Also, as a sample gets larger, it tends to form a vortex ground state but this is not always the case. For example, a square sample can have four magnetic ground states where the net magnetization in each points 90^o from each other, but the direction the magnetization in those ground states can be either along the diagonals or the flats of the sample and still maintain the symmetry of the sample. The larger sample is more likely to have the magnetization point towards the flats which is the buckle state shown in Fig. 2.1b, and a smaller sample is more likely to have the magnetization point towards the diagonals which is the leaf state. If the size of the square were to be made larger, the magnetization would form a vortex instead.

Simulation work done by Cowburn and Welland[8] resulted in Fig. 2.1 which shows the magnetic ground states for a square, $Ni_{80}Fe_{20}$ (permalloy) sample with varying thicknesses and sizes. For the sizes of samples under study (250 nm $\times$ 250 nm $\times$ 10 nm and 210 nm $\times$ 210 nm $\times$ 10 nm), we would expect a vortex ground state but a state more similar to buckle is experimentally seen. This discrepancy will be further discussed with a potential explanation in 4.1.1.

Due to the fourfold symmetry expected in the magnetostatic energy landscape and no expected crystalline anisotropy due to the particles being created using a sputtering process, it has been common to approximate the magnetostatic energy to be

$$E = -\frac{U_o}{2}\cos(4\theta) - \mu H\cos(\theta - \theta_H), \tag{2.5}$$

where U_o is the barrier height when no field is applied, θ is the angle of the magnetization, μ is the magnetic moment of the sample and equal to the $V \times M_s$ where V is the volume

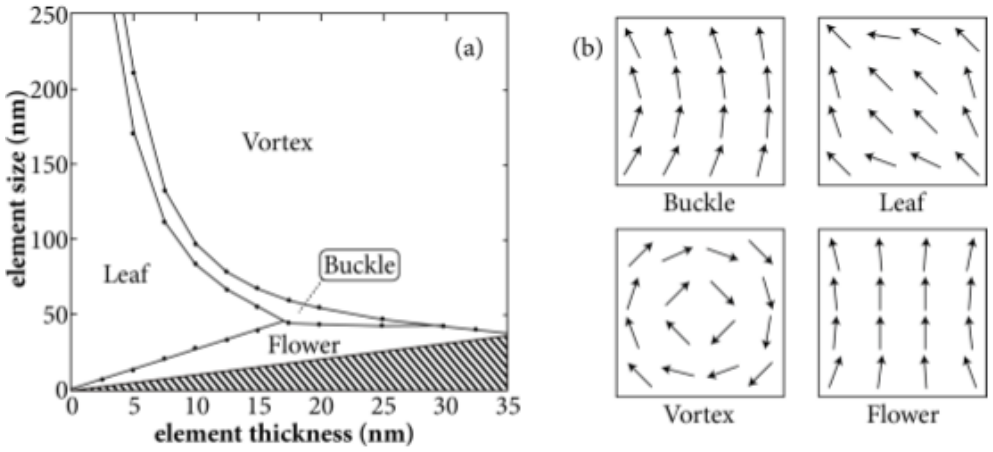

Figure 2.1: a) Phase diagram of the magnetic ground states for a square permalloy sample as the thickness and size are varied.(Reproduced from Cowburn and Welland,[8] with the permission of AIP Publishing.), b) cartoons of each of the four magnetic ground states.

of the sample and M_s is the material's saturation magnetization, and θ_H is the angle of the applied field.[2,9] The characteristics of this form is that the wells are along the flats of the square sample and the barriers are along the diagonals. By including the Zeeman term, when θ_H is along a barrier direction, it has the effect of tilting the energy landscape such that the two minima adjacent to that direction become global minima and the height of the barrier between them can be controlled by changing the magnitude of the applied field. Equation 2.5 can be evaluated to find the height of the barrier for any applied field strength by taking the difference between the magnetization being along the barrier direction, which is on the diagonal, and the well direction, given by

$$E = \frac{U_o}{2}\Big[1 - \cos(4\theta_{min})\Big] - \mu H\Big[1 - \cos\Big(\theta_{min} - \frac{\pi}{4}\Big)\Big], \tag{2.6}$$

where θ_{min} is the angle of the energy minima and must be calculated numerically by minimizing Eq. 2.5. By tilting the energy landscape with an increasing applied field, it changes the location of the well minima and moves them closer towards the barrier as the barrier becomes smaller.

2.1.4 The Hessian Matrix

By combining Eq's. 2.1, 2.3, and 2.4 together in a discrete form shown here

$$E = -2J \sum_{i,j} \left(S_i S_j \cos(\theta_{i,j} - \theta_{i\pm1,j\pm1} - \mu H \cos(\theta_{i,j} - \theta_H) \right) - \\ \frac{\mu_o}{4\pi} \sum_{i,j} \sum_{k,l} \frac{1}{\boldsymbol{r}^3_{i,j\to k,l}} [3(\boldsymbol{m}_{i,j} \cdot \hat{\boldsymbol{r}}_{i,j\to k,l})(\boldsymbol{m}_{k,l} \cdot \hat{\boldsymbol{r}}_{i,j\to k,l}) - \boldsymbol{m}_{i,j} \cdot \boldsymbol{m}_{k,l}], \quad (2.7)$$

the magnetic energy landscape of the sample can be determined. The shape and curvature of the landscape can have drastic changes on the magnetic fluctuations of the system as described by Victora.[10] Using Eq. 2.7, the Hessian matrix, K, a matrix of the second derivatives of the energy with respect to the degrees of freedom of the system can be constructed using

$$K_{i,j} = \frac{\partial^2 E}{\partial \theta_i \partial \theta_j}. \quad (2.8)$$

For the case of our system, the degrees of freedom are the polar angles of each macrospin, θ_i, where the macrospins will be approximated as the unit cells of the simulations that will be discussed in 3.4. Only using the polar angle is based on the assumption that our magnetization always stays within the plane due to the demagnetization fields and is verified by simulations.

Eq. 2.8 results in a matrix that is of size $N^2 \times N^2$ where N is the number of macrospins in the system and will give the curvature of the energy landscape for any possible configuration of the degrees of freedom. To evaluate the Hessian matrix, each of the macrospin's polar angles, θ_i, is replaced with the macrospin's angle obtained from simulation for when the magnetization is in a specific state. A state is defined as the unique configuration of all the macrospins in the system. After K is evaluated for a specific state, it can be diagonalized to obtain its eigenvalues, λ, and their corresponding eigenvectors, v (normal modes). The eigenvalues of K are proportional to the square of their corresponding mode's frequency which amounts to the energy needed to activate that mode. Since the Hessian matrix is Hermitian, all the eigenvalues are real.

Providing a simple example to better convey this concept, we assume a particle that can be described as a 2×2 matrix of spins where all the spins are aligned and the spins only experience the exchange energy between nearest neighbors (see Eq. 2.1). This

results in a Hessian matrix of size 4×4

$$K = \begin{pmatrix} 2J & -J & -J & 0 \\ -J & 2J & 0 & -J \\ -J & 0 & 2J & -J \\ 0 & -J & -J & 2J \end{pmatrix}, \tag{2.9}$$

which we can immediately see is a Hermitian matrix so we expect real eigenvalues. We approximate the exchange constant J as being equal to one and then diagonalize K to obtain both the eigenvalues

$$\lambda_1 = 4; \lambda_2 = 2; \lambda_3 = 2; \lambda_4 = 0, \tag{2.10}$$

and each eigenvalue's corresponding eigenvector

$$v_1 = \{1, -1, -1, 1\}; v_2 = \{-1, 0, 0, 1\}; v_3 = \{0, -1, 1, 0\}; v_4 = \{1, 1, 1, 1\}. \tag{2.11}$$

The first eigenvalue, λ_1, is the largest meaning its normal mode requires the largest amount of energy to excite. When the terms of the eigenvectors are $+1$, that says the corresponding spin will oscillate at the same frequency but 180^o out of phase with a spin that has a corresponding term of -1. This makes it easy to see why v_1 is the highest energy mode. The last eigenvalue v_4 has a value of zero which means its normal mode requires no energy to excite. This is because v_4 is a trivial rotational mode where all the spins rotate coherently with each other which does not cost any energy.

If all the eigenvalues are positive, the energy of the state would be at a local minimum, whereas if all the eigenvalues are negative, the energy of that state is at a local maximum. Much more likely than a maximum though is that there is a combination of positive and negative eigenvalues. This indicates that the state exists as a saddle point where the order of the saddle point is equal to the number of negative eigenvalues. Positive eigenvalues correspond to normal modes that are stable and oscillate while negative eigenvalues correspond to normal modes that are unstable meaning they diverge with time. It is these negative eigenvalues that correspond to possible "paths" that allow the system to transition over the barrier from one minimum to the other.

2.2 Two-State Switching

2.2.1 Kramers' Rate

Consider a two-state system with the states separated by a barrier as shown in Fig. 2.2. We are interested in the time it takes for a particle to leave one well and transition into the other due to thermal fluctuations. This simple model accurately describes many chemical reactions and the behavior of these chemical reactions led Arrhenius to propose his phenomenological equation

$$f = f_o e^{-\frac{\Delta U}{k_b T}}, \tag{2.12}$$

where f is the transition rate, f_o is a characteristic attempt frequency, ΔU is the activation energy (or barrier energy) that the system must overcome to transition, k_b is the Boltzmann constant, and T is the temperature of the system.[11] The characteristic attempt frequency is how many attempts per second a particle in a single well system makes to try and get over the barrier and the exponential term is known as the Boltzmann factor and gives the probability that any individual attempt has enough energy from thermal fluctuations to transition over the barrier. Arrhenius was able to fit his equation to eight independently published collections of data on chemical reaction rates using f_o as his fitting parameter.

This result was largely untouched for decades until work most notably done by Eyring[12] and Kramers[13] who each attempted to provide a more rigorous derivation for Arrhenius's result to take into account the required temperature fluctuations and coupling to a heat bath needed to enable transitions over the barrier. Focusing on Kramers' work, he started from the equation of motion for particles of mass, m, undergoing Brownian motion in a single well as his Langevin equation

$$m\ddot{\boldsymbol{x}} = -U'(\boldsymbol{x}) - \beta m\dot{\boldsymbol{x}} + \xi(t), \tag{2.13}$$

where $\ddot{\boldsymbol{x}}$ and $\dot{\boldsymbol{x}}$ are the acceleration and velocity of the particle respectively, $U'(\boldsymbol{x})$ is the spatially dependent first derivative of the potential energy i.e. the force, β is the damping rate and $\xi(t)$ is a Gaussian white noise term that behaves as

$$\overline{\xi(t)} = 0; \text{ and } \overline{\xi(t_1)\xi(t_2)} = (2m\beta k_b T)\delta(t_1 - t_2). \tag{2.14}$$

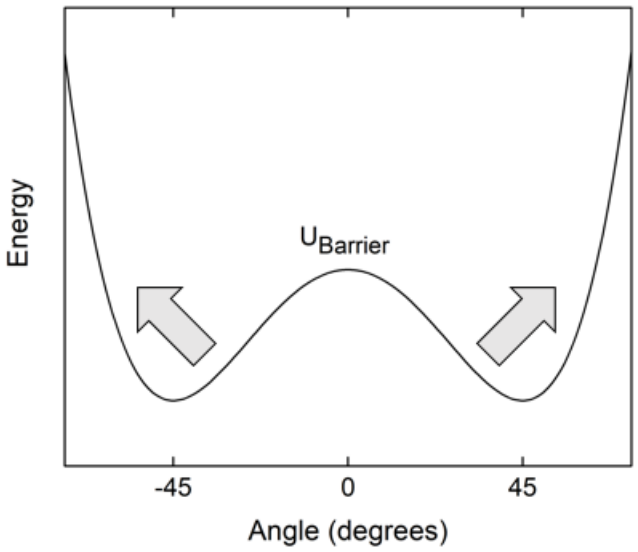

Figure 2.2: Cartoon of a double well system where the energy versus angle landscape is shown. Each well in this cartoon corresponds to the magnetization in a sample being in different directions.

where the bar designates average values. The purpose of the white noise term was to incorporate the necessary connection to the heat bath as a source of thermal fluctuations. The heat bath is coupled to the system through the damping relaxation rate, β; although named the damping relaxation rate, β also describes the effectiveness of the system to absorb thermal energy in addition to dissipation. This means the better a system is at losing energy to the heat bath, the better it is also at absorbing energy from the heat bath which is why β enters the Langevin equation through Eq. 2.14.

Kramers made the assumptions that if the particle cleared the barrier, it was lost to the system, that $U > k_bT$, and that the particles in the well start in a Boltzmann distribution of states (thermal equilibrium) at the bottom of the well. Using Eq. 2.13, Kramers derived the appropriate Fokker-Planck function for the distribution function $p(\boldsymbol{x}, \dot{\boldsymbol{x}}, t)$, also known as the Klein-Kramers equation,

$$\frac{\partial}{\partial t}p(\boldsymbol{x}, \dot{\boldsymbol{x}}, t) = \Big[-\frac{\partial \dot{\boldsymbol{x}}}{\partial \boldsymbol{x}} + \frac{\partial}{\partial \dot{\boldsymbol{x}}}\frac{U'(\boldsymbol{x}) + m\beta\dot{\boldsymbol{x}}}{m} + \frac{\gamma k_b T}{m}\frac{\partial^2}{\partial \dot{\boldsymbol{x}}^2}\Big]p(\boldsymbol{x}, \dot{\boldsymbol{x}}, t). \tag{2.15}$$

When applied to an overdamped system ($\beta > \omega_{\text{well}}$), also known as the intermediate to

high damping regime (IHD), f_o is given as

$$f_o = \Big[\Big(1 + \frac{\beta^2}{4\omega_{\text{barrier}}^2}\Big)^{1/2} - \frac{\beta}{2\omega_{\text{barrier}}}\Big]\frac{\omega_{\text{well}}}{2\pi}, \tag{2.16}$$

where ω_{well} and ω_{barrier} are the characteristic frequencies associated with the curvature at the bottom of the well and top of the barrier respectively, U"$(\boldsymbol{x})|_{x=x_{\text{well,barrier}}}$, and are given by

$$\omega_{\text{well,barrier}} = \sqrt{\frac{U''(\boldsymbol{x})}{m}}\Big|_{x=x_{\text{well,barrier}}}. \tag{2.17}$$

More relevant to our research, when applied to an underdamped system ($\beta < \omega_{\text{well}}$) which is the very low damping regime (VLD), f_o is given as

$$f_o = \frac{\beta S}{k_b t T}\frac{\omega_{\text{well}}}{2\pi}, \tag{2.18}$$

where S is the action of the path the particles take in the well and when combined together with β as βS gives the amount of energy lost per oscillation by the particles in the well. We also point out that $\omega_{\text{well}}/2\pi$ is the characteristic attempt frequency from Transition State Theory, a much simpler model for thermally activated switching which describes the theoretical maximum rate a systen should be able to transition.[14] The other terms in both Eq. 2.16 and 2.18 are damping terms which are unitless factors that account for the excess time it takes for the system to return to thermal equilibrium. Kramers was unable to model the transition rate for damping rates between these two regimes which became known as the Kramers turnover problem.[14] A solution that bridged these two regimes was finally resolved by Mel'nikov and Meshkov almost fifty years later which we will discuss in 2.2.3.

It is important to note that Kramers considered only particles described by a Boltzmann distribution of states, i.e. his model is applicable only after the system has relaxed. Kramers extended his work to a double well system where the particles have excess energy from transitioning over the barrier. He assumed that this excess energy must be lost to the heat bath returning the system to a Boltzmann distribution of states prior to transitioning back over the barrier. For this to occur, the thermalization time, τ_{thermal} must be much shorter than the average time between transitions, τ, which is equivalent to $1/f$.

Equation 2.16 and 2.18 suggest that the more sharp the curvature of the well, the more attempts the system makes to clear the barrier. Since these frequencies are associated with the curvature of the energy, they can also be associated with the entropy of the system since the entropy of the system depends on the shape of the energy as discussed by Skomskii.[15]

2.2.2 Brown's Derivation

Brown extended the work of Kramers to find a solution for the dwell time of a superparamagnetic, uniaxial particle. The uniaxial particle has two ground states where the magnetization can point in either direction of the uniaxial anisotropy and the two ground states are separated by a barrier. Brown used a modified Landau-Lifshitz-Gilbert (LLG) equation with an additional white noise term, $\boldsymbol{h}(t)$, as his Langevin equation resulting in

$$\dot{\boldsymbol{M}}(t) = \boldsymbol{M} \times (\gamma \boldsymbol{H}(t) - \alpha \dot{\boldsymbol{M}}(t) + \gamma \boldsymbol{h}(t)), \tag{2.19}$$

where $\boldsymbol{M}$ is the system's magnetization and $\dot{\boldsymbol{M}}$ is its time derivative, γ is the gyromagnetic ratio and α is the unitless Gilbert damping factor.[5,16–18] The first term of the LLG equation describes the precession of a magnetic spin around an applied field and the second term describes how the precession of that spin decays until the spin is aligned with the field. Brown added $\boldsymbol{h}(t)$ as a time dependent, effective field as a part of $\boldsymbol{H}(t)$ that represents the thermal fluctuations that arise from being coupled to a heat bath. This additional term is required to have the properties

$$\overline{h_i(t)} = 0; \tag{2.20}$$

$$\overline{h_i(t_1) h_j(t_2)} = \frac{2 k_b T \alpha}{V \gamma M_s} \delta_{i,j} \delta(t_1 - t_2), \tag{2.21}$$

where the indices i, j distinguish between the spatial directions, V is the volume of the sample M_s is the saturation magnetization, and the bars represent average values. Equation 2.20 requires that the magnetic noise have an average value of zero and Eq. 2.21 requires that the magnetic noise be uncorrelated in both time and space. Equation 2.21 also gives a scale to the size of the magnetic fluctuations where their strength is proportional to the temperature and inversely proportional to the volume and the

saturation magnetization. The higher the temperature, the more thermally activated noise we expect. The volume and saturation magnetization terms combine to form the energy scale that the temperature has to overcome to create the fluctuations.[19,20]

Using Eq. 2.19 and the assumptions that the system was a uniformly magnetized particle, that the barrier height is much larger than the thermal energies, and the particle returned to thermal equilibrium before transitioning, Brown derived the appropriate Fokker-Planck equation for the distribution function, $W(\theta, \phi, t)$, where θ and ϕ are the angle coordinates of the magnetization. $W(\theta, \phi, t)$ gives the probability of finding the magnetization direction along a unit sphere such that its derivative with respect to the magnetization is given by

$$\frac{\partial}{\partial \boldsymbol{M}} W(\theta, \phi, t) = \frac{1}{2\tau_N} \Big\{ \frac{V}{k_b T} \Big[\alpha^{-1} \boldsymbol{M} \cdot \Big(\frac{\partial V}{\partial \boldsymbol{M}} \times \frac{\partial W}{\partial \boldsymbol{M}} \Big) + \frac{\partial}{\partial \boldsymbol{M}} \cdot \Big(W \frac{\partial V}{\partial \boldsymbol{M}} \Big) \Big] + \Delta W \Big\}, \quad (2.22)$$

where V is the Gibbs free energy density of the particle, Δ is the Laplacian on the surface of a unit sphere and

$$\tau_N = \frac{V M_s (1 + \alpha^2)}{2\gamma \alpha k_b T}, \quad (2.23)$$

where τ_N is known as the Néel time which is an intrinsic time of the system associated with the magnetic noise. It is similar to the mean free time that a particle undergoing Brownian motion experiences and is also sometimes referred to as the free diffusion time. Not needing to assume a particular damping regime due to the polar symmetry of the system, Brown was able to apply Eq. 2.22 to the case of a uniaxial, uniformly magnetized particle with a constant field along the easy axis to obtain the average dwell times, τ, in each well. He then took the limit of those dwell times for the field going to zero to obtain the result for a symmetric, double well particle

$$\tau = \tau_o e^{\frac{U}{k_b T}} = \frac{\sqrt{\pi} \tau_N (k_b T)^{3/2}}{2U^{3/2}} e^{\frac{U}{k_b T}}. \quad (2.24)$$

Incorporating Eq. 2.23 into Eq. 2.24, the prefactor is proportional to $\sqrt{T}$ and decreases as $U^{3/2}$. For nanoscale sized particles, the prefactor has a range in values from 10^9–10^{11} Hz which is close to ferromagnetic resonance (FMR) frequencies and usually researchers assume f_o to be the FMR frequency.[21] For samples of the size under study, τ_o has an approximate value of 5×10^{-5} s at 100 K and barrier height of 170 meV as will be discussed in 4.

2.2.3 Depopulation Factor

From Kramers' derivation in 2.2.1, he found that the prefactors gained an additional damping related term that depended upon which regime of damping the system was in as can be seen from the differences between Eq. 2.16 and 2.18. These damping terms arise from the assumption that the particles must return to thermal equilibrium before being able to transition back over the barrier and are unitless factors that account for excess time it takes for the system to return to thermal equilibrium. Due to this, we will be referring to the terms of f_o from Eq. 2.12 as prefactors to emphasize that they are more complicated than just an attempt frequency. Kramers was unable to develop a crossover model between the two regimes: VLD ($\omega_o > \beta$) and IHD ($\beta > \omega_o$).

Mel'nikov and Meshkov were interested in providing a solution that covered both the VLD and IHD regimes and all damping values between.[22] For a single well, they solved the Kramers turnover problem by using a Green function to solve Kramers' Fokker-Planck equation. The Green function describes the behavior at all levels of damping from the VLD regime to the IHD regime. In their work for a single well system, the damping related correction to the prefactor of Eq. 2.12 is called the depopulation factor, $A(\beta S)$, and replaces the damping related terms in both Eq. 2.16 and 2.18. They take the Fourier transform of the Green function using the Wiener-Hopf method and find $A(\beta S)$ to be given by

$$A(\beta S) = exp\Big(\frac{1}{2\pi}\int_{-\infty}^{\infty} \log\big(1 - e^{-\frac{\beta S}{k_b T}(z^2+1/4)}\big)\frac{dz}{z^2+1/4}\Big), \tag{2.25}$$

where z is the complex part of the Fourier transform of the particle's energy fluctuations, β is a damping term and S is the action and together are a measure of the amount of energy lost per oscillation in the well. A graph of Eq. 2.25 is shown in Fig. 2.3. The depopulation factor, $A(\beta S)$, replaces the damping related terms in both Eq. 2.16 and 2.18 for a single well to give

$$f = A(\beta S)\frac{\omega_{\text{well}}}{2\pi}e^{\frac{-U}{k_b T}}. \tag{2.26}$$

For a particle in a single well, S can be calculated using

$$S = 2\int_{x_L}^{x_R}[-2mU(x)]^{\frac{1}{2}}dx, \tag{2.27}$$

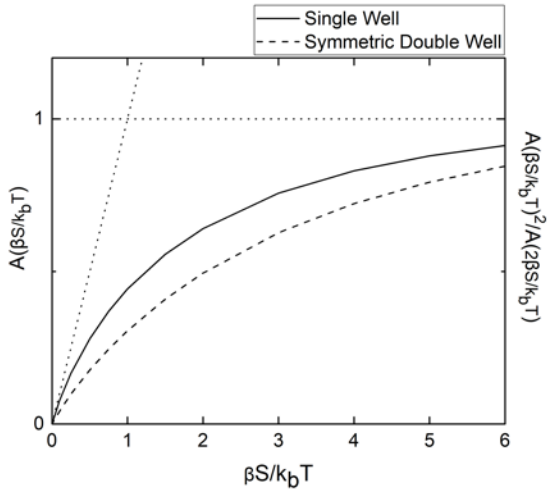

Figure 2.3: A plot of the depopulation factor versus $\beta S/k_bT$ for a single well on the left (solid line) from Eq. 2.25 and for a symmetric double well on the right (dashed line) from Eq. 2.28.[22] The two plots have the same values for the axes. The dotted lines show the trend of the single well depopulation factor at low and high damping. At low damping, the single well term behaves as a straight line with a slope proportional to βS and at high damping it saturates to unity. The double well depopulation factor depends on $A(\beta S)^2$ for two wells of equal energy.

where x_L and x_R are the turning points of the particles in the well with x_L being the turning point to the left of the minimum and x_R being the location of the well maximum and m being the mass of the particles in the well. According to Mel'nikov and Meshkov, S is well approximated by U/ω_o; within an order of magnitude.

As can be seen in Fig. 2.3, $A(\beta S)$ for a single well approaches unity at very high damping rates which recovers Eq. 2.16 in the high damping limit and has a slope that is proportional to βS at very low damping rates which recovers Eq. 2.18. The smaller the value of $A(\beta S)$, the shorter the transition rate as seen in Eq. 2.26. As $A(\beta S)$ increases towards unity, Eq. 2.26 restores the Transition State Theory solution which is the fastest a system can transition. This means the damping terms can only reduce the transition rate which comes from the fact that the particles must lose their excess energy before transitioning and this requires the particle spend longer in the well. This means that the depopulation factor can never cause the switching rate to be faster than

the simple solution.

Mel'nikov and Meshkov extended their calculation to a double well system for the VLD regime where a particle can leave one well and, before reaching thermal equilibrium, hop back over the barrier into the first well. The result they obtained is

$$A(\beta S_1, \beta S_2) = \frac{A(\beta S_1)A(\beta S_2)}{A(\beta S_1 + \beta S_2)}, \tag{2.28}$$

with a plot shown in Fig. 2.3 for a symmetric double well system (both wells being the same depth). Despite Mel'nikov and Meshkov claiming that the particle should be able to hop back faster with its extra energy from the transition over the barrier, Eq. 2.28 suggests that the double well system actually has transitions that are slower than the transitions in a single well. By comparing the behavior of a single well to that of a double well in Fig. 2.3, we see that the curve is lower for the same value of $\beta S/k_bT$ for the double well system than for the single well which means $f_o A(\beta S)$ is smaller i.e. slower transitions.

Despite Brown not needing to account for a particular damping regime in his derivation in 2.2.2 due to the symmetry of the system, according to Coffey et al.,[18] it is still necessary to apply the depopulation factor from Eq. 2.25 to Eq. 2.24 because the time needed to absorb and dissipate the thermal fluctuations needs to be taken into account. To calculate the depopulation factor for a magnetic particle directly, the magnetic action derived by Klik and Gunther[23] is used and is given by the contour integral

$$S = \oint \frac{1-\cos^2\theta}{-\sin\theta}\frac{\partial U}{\partial \theta}d\phi - \frac{-\sin\theta}{1-\cos^2\theta}\frac{\partial U}{\partial \phi}d\theta, \tag{2.29}$$

where θ and ϕ are the polar and azimuthal angles of the magnetization and the path of integration is known as the separatrix. To obtain the separatrix, the lines of equipotential for the energy of a single well system, $E(\theta, \phi)$, must be determined. Energies smaller than the barrier height of the single well will have closed equipotential lines and energies larger than the barrier height will have open equipotential lines. This means that closed equipotential lines represent the maximum trajectory that any bound particle with some energy in the well can have. Open lines show the trajectory that particles with larger energy than the barrier height can take which allows them to escape the well. The separatrix is the closed line with the largest energy which is equal to the barrier height. When the magnetic action, S, is multiplied by α, which is the unitless

equivalent of β in magnetic systems, the product gives the amount of energy lost per oscillation.

For a magnetic system with cubic anisotropy,[24] S is found to be

$$S = \frac{8\pi U}{9}, \tag{2.30}$$

or $\approx U$. For ferromagnetic systems, the VLD regime is when $\alpha << 1$ and the IHD regime occurs when $\alpha > 1$. The damping factor for a ferromagnetic system is the Gilbert damping factor, α, and always has values less than one[25] and for the system under study, $\alpha = 0.01$ which is sufficiently small to consider our system to be in the VLD regime.[26]

Knowing both the action and the damping, we are able to calculate the average number of oscillations in a well the system needs to reach thermal equilibrium. Since the energy lost per oscillation is αS and the barrier height is U, the number of oscillations needed to thermalize is found by dividing the latter by the former, or $1/\alpha$. The total time needed to reach thermal equilibrium, τ_{thermal}, is the product of the number of oscillations and the characteristic dwell time, τ_o, from Eq. 2.24 which is also the time for one oscillation to occur. The thermalization time is then given by

$$\tau_{\text{thermal}} = \frac{\tau_o}{\alpha}. \tag{2.31}$$

This will be useful in 4.2.4 when discussing whether or not we are in thermal equilibrium when we transition.

2.2.4 Multidimensional Solution

For the work done by Brown described in 2.2.2, he assumed that the uniaxial particle was uniformly magnetized and acted as a macrospin. For large particles, this assumption would not be valid. In this case, we must consider how macrospins smaller than the size of the particle but larger than the exchange length are attempting to transition over the barrier where each macrospin is a separate degree of freedom for the system.

After calculating the Hessian matrix as explained in 2.1.4, the system states can be found using simulations of the system at a minimum and along the saddle point. The angle of each macrospin at either the minimum state or the saddle point state $(\theta_1, \theta_2 \ldots \theta_N)$ are placed into the Hessian matrix and then it is diagonalized giving both

the eigenfunctions and the eigenvalues λ. All eigenvalues $\lambda > 0$ represent stable modes and all values $\lambda < 0$ represent unstable modes. These systems tend to have only one unstable mode associated with the saddle point. Using this approach, the switching rate for a system of N vibrational nodes is[27]

$$f \propto \frac{1}{2\pi} \frac{\Pi_i^N \lambda_i^m}{\Pi_i^{N-1} \lambda_i^s} e^{\frac{-U}{k_b T}}, \tag{2.32}$$

where λ^m are the eigenvalues of the minimum and λ^s are the eigenvalues of the stable modes of the saddle point.

In their review paper, Coffey and Kalmykov consolidated the work of others when it came to applying this multidimensional solution to physical systems.[14,27–29] Equation 2.32 is derived using the flux-over-population method[30] which says that the rate of fluctuations over the barrier are proportional to the current of particles moving across the barrier, j, divided by the number of particles starting in the well in a Boltzmann distribution of states, n. Both j and n are proportional to the partition function for particles existing near the saddle point and well minimum respectively

$$j \propto \oint e^{\frac{-U_{\text{saddle}}}{k_b T}} dS; n \propto \oint e^{\frac{-U_{\text{well}}}{k_b T}} dA, \tag{2.33}$$

which are the surface integrals of the Boltzmann distribution where S in this case is the area around the saddle point and A is the area of the well. To solve these equations, it becomes necessary to expand U for small oscillations around the saddle point and well minimum respectively because we are only interested in what the system is doing near those two locations. With this expansion, the integrals become solvable with the result given by

$$j \propto e^{-\frac{U_{\text{saddle}}}{k_b T}} (\Pi_i^{N-1} \lambda_i^s)^{-1}; n \propto e^{-\frac{U_{\text{well}}}{k_b T}} (\Pi_i^N \lambda_i^m)^{-1}, \tag{2.34}$$

where the products of eigenvalues are equal to the determinants of the Hessian matrix at the saddle point and well. The product of eigenvalues for current, j, goes to $N-1$ due to the fact that a saddle point will have one unstable mode that is not used for this product. The rate of transitioning over the barrier is given by

$$f = \frac{j}{n} = \frac{\Pi_i^N \lambda_i^m}{\Pi_i^{N-1} \lambda_i^s} e^{-\Delta U}, \tag{2.35}$$

with ΔU being the difference in energies between the saddle point and well i.e. the barrier height, which gives the same solution as given by Eq. 2.32.

In the VLD regime, it is possible that the particles in the system keep much of their excess energy from each transition since it takes a relatively long amount of time to remove that energy compared to their transition time. If this is the case, the particles spend an appreciable amount of their time near the saddle point instead of near the well minimum. Because the particles are near the saddle point, they have a higher chance of transitioning back over the well early. In 1987, Talkner was able to derive the result for the multidimensional solution in the VLD regime

$$\tau_o \propto \frac{\det(K^s)}{\det(K^m)}, \tag{2.36}$$

where K^s and K^m are the Hessian matrix derived in Eq. 2.8 evaluated at the saddle point and well minimum respectively.[31] The determinant of these matrices are equivalent to the product of eigenvalues in Eq. 2.32, but the physical interpretation is different from the flux-over-population method described previously. In this derivation, the dwell times are inversely proportional to the ratio of the number of particles near the saddle point compared to the number of particles near the well minimum. The larger the fraction of particles that are near the saddle point, the faster the system transitions because those particles almost have enough energy to transition. Just like the previous method, the number of particles near each location in the well are

$$n_s \propto (\Pi\lambda^s)^{-1}; n_m \propto (\Pi\lambda^m)^{-1}. \tag{2.37}$$

2.2.5 Detailed Balance

Detailed balance was first described by Boltzmann in 1872 as an extension of microscopic reversibility.[32] In his picture, if a system has a certain probability of transitioning from a state i into a state j

$$P_{i\to j} = e^{\frac{U_i}{k_b T}}, \tag{2.38}$$

then that is related to the probability of transitioning from j back into i such that

$$\frac{P_{i\to j}}{P_{j\to i}} = e^{\frac{U_i - U_j}{k_b T}}. \tag{2.39}$$

Since microscopic reversibility requires time reversal symmetry, $P_{i\to j}$ and $P_{j\to i}$ can be thought of as the same process but with the direction of motion reversed. Applying this

to a system undergoing thermally activated, two-state switching as described by Eq. 2.24, we can rewrite Eq. 2.38 and 2.39 in those terms

$$\frac{\tau_1}{\tau_o} = e^{\frac{U_1}{k_b T}}; \frac{\tau_1}{\tau_2} = e^{\frac{(U_1 - U_2)}{k_b T}}, \tag{2.40}$$

assuming that τ_o is the same for both wells.

If a magnetic field is applied to the system, time reversal is broken and detailed balance must be modified from Eq. 2.39. In this case, a determination of the effect of a reversed magnetic field on the states j and i must be made; these states will be referred to as j^* and i^*. This is followed by replacing the probability of switching from j to i, $P_{j\to i}$, in Eq. 2.39 with what the probability would be switching from j^* to i^*, $P_{j^*\to i^*}$

$$\frac{P_{j\to i}}{P_{j^*\to i^*}} = e^{\frac{(U_1 - U_2)}{k_b T}}. \tag{2.41}$$

If this step weren't done, the left side of Eq. 2.39 would not be equal to the right side and it would appear that detailed balance was being violated.[33]

2.2.6 Examples of Measuring Two-State Switching

There have been multiple studies performed measuring the rate of two-state switching in ferromagnetic systems. These studies though were done on either collections of particles or on more complicated systems.

Krause et al.[21] measured two state switching in nanoparticles of various shapes and sizes using spin-polarized, scanning tunneling microscopy. They measured characteristic attempt frequencies in their samples from 10^{13} Hz to 10^{16} Hz which depended on the size of the barriers with their data shown in Fig. 2.4. The barrier sizes depended upon the size of the nanoparticles. They determined that the magnetic switching behavior was caused by nucleation and propagation of domain walls in the nanodots and that the larger the size of the nanodot, the more nucleation sites that existed allowed the characteristic attempt frequency to be higher.

Using AC susceptibility measurements, Respaud et al.[34] measured collections of noninteracting, cobalt nanoparticles of average size 2 nm. They found that the measured characteristic stay time to be 4×10^{-12}s. They attributed this behavior to intrinsic properties of the nanoparticles which they did not elaborate on.

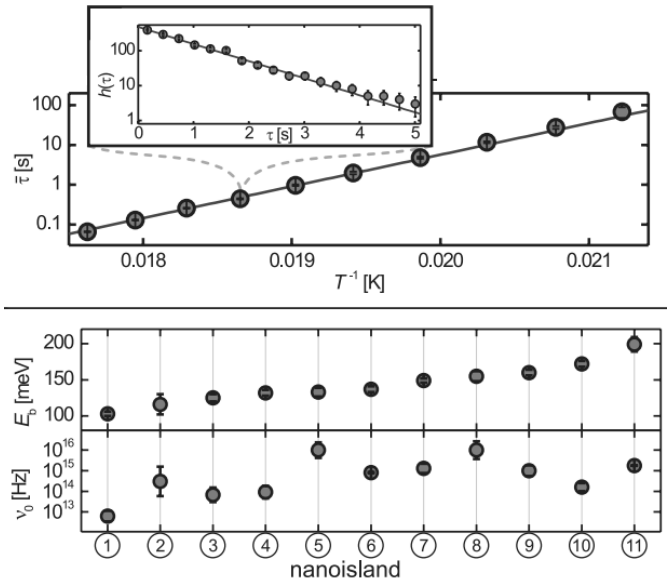

Figure 2.4: First image shows average dwell times, $\bar{\tau}$, as a function of inverse temperature with an example histogram showing how they calculated $\bar{\tau}$. The second image shows both Krause et al.'s measured barrier heights, E, and their characteristic attempt frequencies, ν_o as a function of sample number. (Reproduced and modified with permission.[21])

The system under study for this thesis has also been studied by Endean et al.,[9] Youngblood,[2] and Costanzi.[3] Although not the focus of their research, both Endean and Youngblood noticed characteristic attempt frequencies much higher than expected by either the FMR frequencies or from Brown's result in Eq. 2.24.

2.3 Anisotropic Magnetoresistance

The samples under study are too small for traditional magnetometry so a transport measurement technique was used instead. The resistance of ferromagnetic materials is dependent upon the relative angle between the magnetization direction and current direction in the sample. This effect is known as the anisotropic magnetoresistance (AMR) and was first seen by Lord Kelvin in 1857[35] and explained by Potter and McGuire in 1975.[36] For most materials such as permalloy, the resistance is a maximum when the

two are collinear and a minimum when they are perpendicular. For a small number of materials, the opposite is true. This behavior is commonly described using the following equation

$$R = R_{\perp} + \Delta R \cos^2 \theta, \tag{2.42}$$

where $R_{\perp}$ is the resistance when the magnetization and current directions are perpendicular, ΔR is the difference between $R_{\perp}$ and $R_{\parallel}$, and θ is the angle between the magnetization and current directions.[37] This gives a method of using the resistance of the sample to determine the magnetization direction. Because Eq. 2.42 depends on the square of the cosine, there are two minima and two maxima for a full rotation of the magnetization. Since in our work, a magnetic field is applied, only the magnetization directions within 90^o of the applied field directions are relevant because the two minima next to the barrier being reduced become global minima.

By measuring the AMR of the sample, a field sweep along any direction can be performed to obtain hysteresis loops or a static field can be applied and time records of the resistance can be also measured. Both measurements were performed for the purpose of this study.

AMR is caused by scattering between electrons from the majority spin species in the s orbitals into the minority spin half of the d orbitals in a material through the spin-orbit interaction (SOI) as shown in Fig. 2.5a. The SOI is proportional to $\boldsymbol{L} \cdot \boldsymbol{S}$ so if $\boldsymbol{L}$ is collinear with $\boldsymbol{S}$, the SOI is at a maximum and scattering may be present. If perpendicular, there is no scattering and thus resistance is at a minimum. The d orbitals are essentially locked in place by the crstalline lattice, but the current $\boldsymbol{J}$ is able to propogate along any direction. Via this scattering process, electrons scattering from the s orbitals can only scatter into d orbitals where $\boldsymbol{L}$ is perpendicular with $\boldsymbol{J}$, or in other words, when the momentum of the electrons are in the plane of the d orbital being scattered into. If $\boldsymbol{J}$ is perpendicular with $\boldsymbol{L}$ of an occupied d orbital as seen in Fig. 2.5b, there are less unoccupied d orbitals for the electrons to scatter into. But if $\boldsymbol{J}$ is parallel to $\boldsymbol{L}$ for an occupied d orbital which is shown in 2.5c, there will be empty d orbitals for the electrons to scatter into. For most ferromagnetic materials, $\boldsymbol{L}$ of the occupied d orbitals is parallel with $\boldsymbol{M}$. This results in increased scattering when $\boldsymbol{J}$ is collinear with $\boldsymbol{M}$ than when they are perpendicular.[36,38]

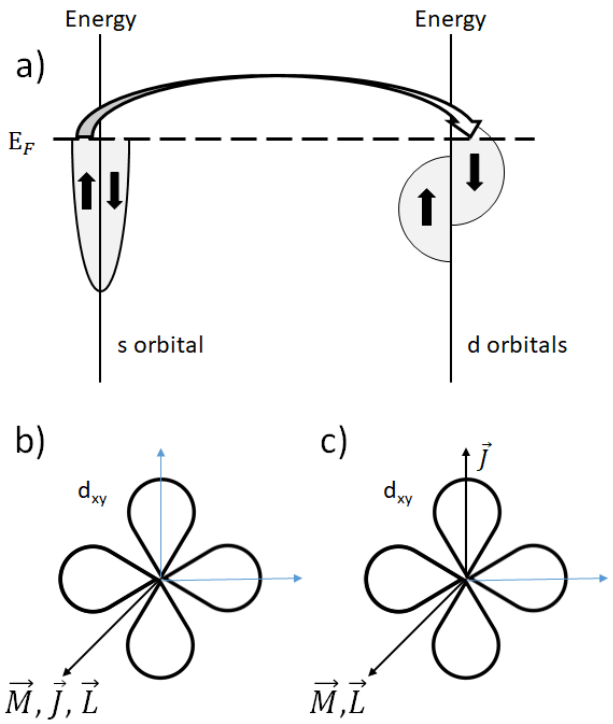

Figure 2.5: AMR scattering process. a) shows the process of majority spin electrons scattering from the s orbital into open d orbital states through the spin-orbit interaction which allows the spin of the electron to flip. b) shows the current perpendicular to the plane of an occupied d orbital. c) shows the current in the plane of an occupied d orbital.

Chapter 3

Experimental Methods

3.1 Sample Preparation

3.1.1 Overview

Our samples were deposited onto Silicon Nitride substrates using a combination of lithography techniques and sputtering deposition. The lithography processes and contact deposition were all performed using equipment in the Minnesota Nano Center (MNC). Actual deposition of the sample material was performed in-house using an ultrahigh vacuum sputtering system. To fabricate the samples, large contacts and alignment marks were created onto the substrate. This was then followed by fabricating the samples themselves and finished by fabricating fine contacts that connect the large contacts to the samples. A cartoon of a sample with contacts is shown in Fig. 3.1.

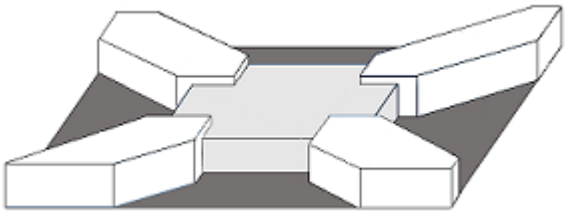

Figure 3.1: Cartoon of a sample with contacts. The dark grey portion is the sample substrate, the light grey portion is the sample, and the white portions are the electrical contacts.

3.1.2 Large Contacts and Alignment Marks

The purpose of the large contacts is to provide a section large enough for wirebonding leads on one end, and a section on the other end at the minimum size limits of optical lithography. Each substrate was patterned with nine sections of sixteen contacts arranged as shown in Fig. 3.2. Each section can have four samples with four contacts going to each sample and the samples are spaced such that the distance between them is much larger than their size to prevent interactions. The four contacts allowed for four terminal measurements of the sample resistance. Along with the large contacts, two sets of alignment marks were patterned onto the substrate. The larger alignment marks were placed at the outer corners of the nine sections which allowed for gross alignment of the substrate for electron beam lithography, whereas the small alignment marks in the inner portions of each of the nine sections were for fine alignment.

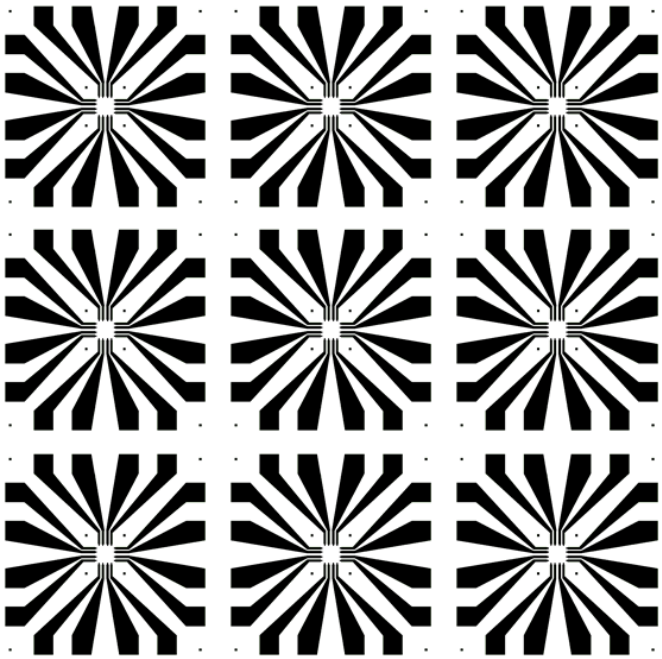

Figure 3.2: Cartoon of the bulk contacts and alignment marks. There are nine sections that will each hold four samples. The gross alignment marks are at the four outer corners of each section and the inner squares of each section are the fine alignment marks. At the center of each section is the area that is designated for the samples and fine contacts.

To fabricate the large contacts and alignment marks, the substrate was first cleaned using acetone/methanol/isopropanol (IPA). Then a photoresist bilayer of polydimethylglutarimide (PMGI) followed by a Microposit 1800 series photoresist was spun onto the substrate. The pattern was created in the photoresist by exposing the substrate to UV light in a Karl Suss MA-6 contact aligner before being chemically developed; 30 nm of titanium is deposited as a seed layer using electron beam evaporation followed by 70 nm of gold. The substrate was then placed into a chemical lift-off that left the large, gold contacts and alignment marks.

3.1.3 Samples

The samples are square dots made of $Ni_{80}Fe_{20}$ (permalloy) that are 250 nm or 210 nm on a side and 10 nm thick. Permalloy was chosen for being magnetically soft with low crystalline anisotropy and for having a relatively large anisotropic magnetoresistance.[38] The sample is a trilayer with a 3 nm seed layer of tantalum, 10 nm permalloy and capped with a 3 nm layer of ruthenium to prevent oxidation of the permalloy. The seed layer was used due to permalloy's poor adhesion to the insulating substrate and the capping layer was chosen because its oxide is also a conductor which reduces the resistance between the contacts and the sample reducing the Johnson-Nyquist noise. A cartoon diagram of the sample layout with attached contacts is shown in Fig. 3.3.

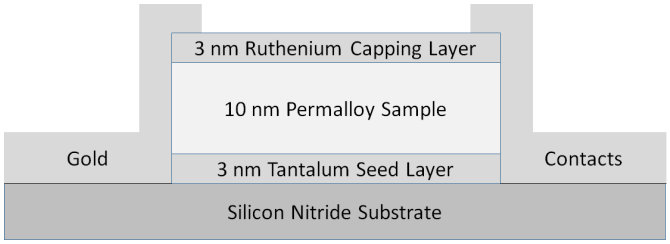

Figure 3.3: Cartoon of the sample layers and attached contacts.

The substrate with large contacts and alignment marks was cleaned using acetone/methanol/IPA. A photoresist layer of polymethylmethylacrylate (PMMA) was then spin coated onto the substrate. Electron beam lithography using a Vistec 100kV EBPG-5000 (Vistec) was used to pattern the samples using an aligned write. The

pattern was chemically developed for forty seconds using 3:1 Methyl isobutyl ketone (MIBK)/IPA and the development was then stopped by placing the substrate in IPA for sixty seconds. To deposit the material for the samples, the developed substrate was placed into our in-house sputtering system. The 3 nm of tantallum, followed by the 10 nm of permalloy, and lastly, the capping layer of 3 nm ruthenium are deposited onto the substrate. The substrate was placed into a mixture of 1:1 acetone/N-Methyl-2-pyrrolidone (NMP) for a minimum of thirty minutes which chemically removed the photoresist and the deposited material that was on top of it leaving the samples in the areas where the photoresist was removed via development. A consequence of this method is that it leaves excess metal (fencing) on the edges of the sample. This can result in unwanted magnetic structure so to rectify this, the fencing was removed in an Intlvac Ion Mill which etched away material from the sample using an ionized argon beam.

Using this method, relatively uniform and consistent samples can be made for testing.

3.1.4 Fine Contacts

After sample deposition, the large contacts must be connected to the samples with fine leads. The fine leads are made of a 5 nm seed layer of $Ti_{90}W_{10}$ followed by a 25 nm layer of gold. The purpose of the fine contacts is to connect the smaller end of the larger contacts to the samples. Each contact overlays on top of the samples with a 50 nm x 50 nm area to ensure connectivity and for the contacts to be far enough apart to prevent shorting. Using this design resulted in a yield of electrically connected samples of about 80%.

After the samples were fabricated onto the substrate as described in the previous section, the substrate was then cleaned again in acetone/methanol/IPA. A bilayer resist of PMMA as the bottom layer and PMGI as the top layer was coated onto the substrate. Having a thicker photoresist helps ensure better liftoff of the contacts without leaving any gold on top of the samples which would result in electrically shorting the samples. It also gave a better resolution when depositing material to ensure that there was sufficient overlap with the samples to ensure electrical connectivity. The Vistec was once again used to perform an aligned write of the fine contact pattern. Due to the nature of

the way aligned writes work with the Vistec, the first gross alignment mark became overexposed when patterning the samples. This is a result of the Vistec having to search for the first gross alignment mark used using the electron beam. This search for the gross alignment mark continuously exposes the photoresist around that alignment mark. To overcome this, alignment must take place with the other three gross alignment marks.

The pattern was then chemically developed in tetramethylammonium hydroxide and water (CD-26) for forty seconds and the development was stopped by placing it in water for sixty seconds. While developing the pattern, not all of the developed resist will be removed along the side of the samples. If it is not removed, it will act as an insulator and the fine contacts won't be able to connect to the samples. The substrate was placed back into the Intlvac Ion Mill where this residual resist is removed. The substrate was then placed into an AJA sputter system where the 5 nm $Ti_{90}W_{10}$ seed layer is deposited followed by 25 nm gold contacts. The substrate was then placed into acetone/NMP for thirty minutes for chemical liftoff. If any excess material remains, the substrate was sonicated in 1:1 NMP/acetone using a Cole-Parmer 8890 sonicator at 100 V for five minutes to forcibly remove the excess without damaging the samples.

3.2 Experimental Setup

3.2.1 Cryostat

A substrate with the samples was mounted onto a sample holder using a thin layer of Apiezon-N Grease for thermal conductivity and adhesion of the substrate to the sample holder. The sample holder has contacts which were wirebonded to the contact pads on the substrate using aluminum wire. The holder was then connected to the cold head of an Advanced Research Systems Inc. 4K Cryostat. The cryostat uses a closed-cycle helium compressor to cool the sample down to 4 K. There were two methods of temperature control used. First, if a steady state temperature above 4 K was desired, a fixed current was supplied to a 50 Ω heater attached to the cold head which allowed the sample temperature to be controlled between 4 K and room temperature. The current to the heater was provided by a Kepco bipolar power supply and controlled manually. The second method was to turn off the compressor and to let the cryostat warm up

which is how all measurements made over a temperature range were taken.

3.2.2 Thermometry

There are two thermometers inside the cryostat for determining both the sample temperature and for temperature control. The first thermometer is a GaAlAs diode which is mounted to the cold head of the cryostat near the heater. This thermometer can be used for both temperature control and as a backup indication for the sample temperature. The second thermometer is a calibrated Cernox thermometer which is mounted to the side of the sample block and closely agrees with the actual sample temperature as verified by measuring the temperature dependent resistance of a resistor mounted to the sample holder. Both of these thermometers are connected to Kiethley 2000 multimeters for data collection.

3.2.3 Electromagnet

A Cenco electromagnet was used to apply a magnetic field in plane of the sample. The electromagnet is positioned such that the sample holder attached to the cold head is directly between the pole faces. The electromagnet was placed on top of a turn table with precision angular control so that the direction of the field can be controlled. The current to the electromagnet was provided by a Kepco bipolar power supply which allows the electromagnet to reach fields of up to 400 Oe. The power supply was controlled by a computer via a digital to analog converter.

3.2.4 Data Recording

A constant DC current was provided to a sample and the sample voltage was measured after first being amplified with a Stanford Research Systems low-noise preamplifer which was AC coupled. This allowed the signal to be amplified with a gain of 10^4 and thus reduce the influence of any noise by subsequent electronics. The AC coupling removed the DC bias of the signal which, if amplified, would exceed the preamplifier's maximum voltage output. The amplified signal was next passed through a Krohn-Hite eight pole, Butterworth low-pass filter. The low-pass filter was set to 45 kHz to keep it less than half the desired sample frequency of 100 ksamples a second to prevent Nyquist aliasing.[39]

This also aided in limiting the white noise and thus improving signal to noise ratio. The frequency setting does have the effect of removing any frequency signal near and above 45 kHz which puts an upper constraint on the fastest transitions measurable. Next, the filtered and ampified signal was sent to a Tektronix digital oscilloscope for analog to digital conversion. The oscilloscope was set to record at 100 ksamples per second for 10 seconds. The time length was chosen to ensure enough transitions were recorded even for when the sample was undergoing slow transitions ($\approx$ 0.1 seconds). The sampling rate was chosen for data processing time considerations and also allows transitions on the order of 10^{-5} seconds to be measured. Lastly, the digital signal was sent to a computer for recording and calculations.

3.2.5 Data Processing

Using Labview, the DC voltage data was grouped with the temperature data and the time. The data was then processed using Python to calculate the average time the data stayed in either the high resistance state or the low resistance state before transitioning. This resulted in two averaged values, one for each state, and the temperature of the sample undergoing the transitions. The average times at different temperatures were plotted on a semilog plot versus the inverse temperature and an exponential fit of Eq. 2.12 was performed to determine both the prefactor and the barrier height for each state.

3.3 Operation

3.3.1 Measuring Barrier Heights

When measurements were started on a new sample, the barrier heights of each well were measured first. The field was applied along one of the flats of the sample and the magnetization was saturated in that direction. This placed the magnetization direction into the minimum well along that direction. The field (0^o) was then reduced to zero and the magnet was rotated 90^o. The field was then increased until the resistance abruptly changed and the field strength was recorded. This coincided with the magnetization direction leaving one minimum and moving into the minimum along the field direction

with the resistance change due to the anisotropic magnetoresistance (AMR). The magnetization was then saturated along the field direction before the field was returned to zero. The magnet was rotated back to its initial position and the field was increased until again, the resistance abruptly changed. The strength of the field was then recorded again. The field strength at which the resistance switched, H_{switch}, could then be used to calculate that well's barrier height using[9]

$$U = \frac{V M_s H_{\text{switch}}}{4}, \tag{3.1}$$

where M_s is equal to 800 emu/cm^3.[38]

This process was repeated at regular intervals of the field directions between 0-90^o. At 45^o, the resistance continuously changed with increasing field until the resistance saturated. This occurs because the applied field supplies no torque to move the magnetization into the other well, instead forcing it to point towards the barrier direction only.

3.3.2 Fractional AMR Signal

The parallel and perpendicular resistances for Eq. 2.42 were measured by saturating the magnetization of the sample along 0^o and then 90^o and the resistance recorded for both cases. The difference in resistance, ΔR, gave the maximum AMR signal size for the sample. The magnetization was then placed into one of the two wells and the field was applied along 45^o and slowly increased. At regular intervals in the field strength, the resistance, R_1, was recorded until the sample underwent two state switching. The magnetization direction was then placed in the other well and the field increased along the diagonal. The resistance for that well, R_2, was measured at the same fields as before. At each field strength, the difference in resistances was compared to the maximum AMR signal size to give a fractional AMR signal. Based on Eq. 2.42, the difference in resistances at a given field strength can be written as:

$$R_1 - R_2 = \Delta R[\cos\theta - \cos(\pi/2 - \theta)], \tag{3.2}$$

which can be compared to the total AMR signal size which results in the fractional AMR signal:

$$\text{AMR}_{\text{fraction}} = \frac{R_1 - R_2}{\Delta R} = \frac{V_{\text{fraction}}}{V_{\text{total}}}[\cos\theta - \sin\theta]. \tag{3.3}$$

The volume terms were added because the volume fraction of the dot that actually contributes to the AMR signal size decreases with increasing field. As the field is increased along the diagonal, more of the spins align with the direction of the applied field. The spins in this increasing fraction of the sample is the same for a given field strength regardless of which well the magnetization started in. That means that this fraction of the sample volume does not contribute to any differences in the measured resistance and must be ignored. This process was performed at various temperatures where a temperature dependence was noticed which will be discussed in 4.1.2.

3.3.3 Voltage versus Time Records

To observe two state switching, the sample was cooled down to less than 60 K and then allowed to slowly warm up. Below 60 K, transitions could not be recorded as signal size decreases with temperature and becomes of similar size as the Johnson noise. The decrease in signal size results from colder temperatures requiring a larger barrier reducing field to allow two state switching to occur. But as the field is made larger, a smaller fraction of the dot undergoes two state switching reducing signal size, and also the two wells move closer to the barrier and to each other reducing the difference in resistance between the high and low states.

When the sample warmed up to above 60 K, the field strength was increased along 45^o until two state switching was observed. An example of a measurement of two-state switching is seen in Fig. 3.4. Most samples underwent two state switching at these temperatures near 150 Oe. It was oftentimes necessary to adjust the angle of the applied field by at most a few degrees to observe the switching. We believe this to be due to the samples not being perfectly square and thus the two wells not being the exact same depth.

When switching was observed, the angle of the field was adjusted so that the dwell times for both wells are similar, usually on the order of a tenth of a second for each. When this condition was met, 10 second recordings of the sample voltage, temperature, and time (time records) were recorded. These measurements were continued until the switching frequency of at least one of the wells approached the low-pass filter cutoff frequency. When this occurred, the field strength was lowered and the angle adjusted as necessary to make both states' dwell times similar. Then a new collection of time

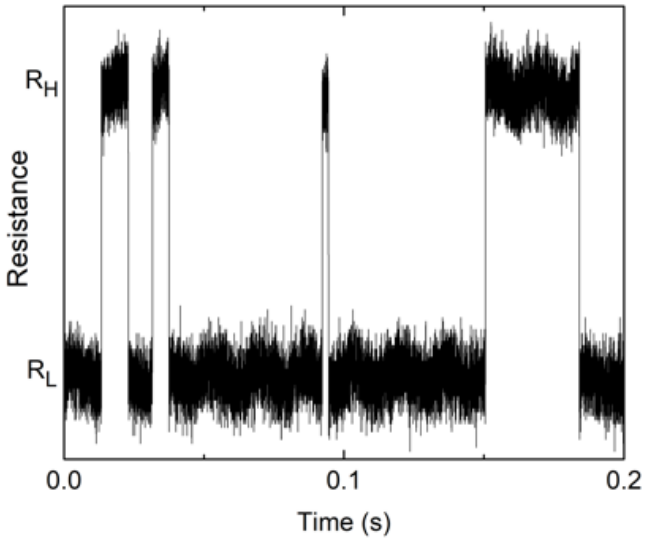

Figure 3.4: Time record of two-state switching where the resistance fluctuates randomly between two resistance states.

records was started. This process was repeated up to room temperature, resulting in multiple collections of time records for the same sample. As the samples warmed, the range of temperatures increased so that time records could be collected without needing to adjust the field angle or strength. As the temperature approached room temperature, any change in sample temperature is a smaller fractional change and thus has a smaller effect on the switching frequency. The result is that near 60 K, time records could be collected over 10 K ranges, but near room temperature, time records could be collected over 40 K ranges.

Only the averaged dwell times from each collection of time records were used together for determining prefactors and barrier heights at that field and temperature for that sample as described in 3.2.5.

3.4 Micromagnetic Simulations

Simulations of magnetic relaxation were performed using LLG Micromagnetics Simulator v2 due to its ability to perform AMR measurements and to provide the direction

cosines of the magnetization for each unit cell.[40] Thermally driven switching of the magnetization as a function of time simulations were performed using MuMax3 to take advantage of that program's increased simulation speed at the cost of potential rounding errors due to the number of iterations needed.[41] A square sample of dimensions 250 nm × 250 nm × 10 nm was simulated with a number of unit cells ranging from 50-85 × 50-85 × 2-3. The range in number of unit cells was due to time contraints of subsequent analysis programs. The parameters used were a saturation magnetization of 800 emu/cm^3, an exchange stiffness of 1.05 $\mu erg/cm$, a resistivity of 15 $\mu\Omega \cdot cm$, and a uniaxial anisotropy of 0 erg/cm^3 as appropriate for permalloy with no crystalline anisotropy.[38] Simulations were performed at both 0 K and at various temperatures up to 300 K. The length scales of the cell size were chosen to be smaller than the exchange length in permalloy having no crystalline anisotropy or 5.7 nm as derived by

$$l_{\text{ex}} = \sqrt{\frac{A}{K_u + 2\pi M_s^2}}, \tag{3.4}$$

where A is the exchange stiffness and K_u is the crystalline anisotropy.[38]

To simulate the AMR, a 100 μA current was sourced to one corner of the sample and drained through an adjacent corner. Both LLG Micromagnetics Simulator and Mumax3 numerically solve the Landau-Lifshitz-Gilbert equation for each cell in the simulation and through a relaxation method, derives the magnetic states of the sample. Temperature effects can be added along with a magnetic field of any magnitude and direction. The simulations can be allowed to relax with one field and then the field changed to see how changing the field direction or strength will change the magnetic states.

Using the LLG Micromagnetics Simulator, simulations were made for hysteresis loops of the sample, magnetic states with either an applied field or zero applied field, and examples of two state switching. From the simulations of the magnetic states with and without a field, a calculation of the barrier heights can also be performed. A discretized form of Eq. 3.1 can be created which when used together with the simulations, find an approximate value of the barrier heights as a function of applied field.

$$U = \frac{vM_sH_B}{4} \sum_i \sin \alpha_i \tag{3.5}$$

v is the discretized volume of the simulation, H_B is the barrier reducing field, and α_i is the angle of the spins in the discretized volume derived from the direction cosines of the magnetization calculated by LLG Micromagnetics Simulator.

Chapter 4

Results and Discussion

4.1 Magnetic States

4.1.1 Hysteresis Loops

According to Cowburn et al.[7] for the dimensions of the samples under study, it is expected for the ground state to be a vortex. In fact, both vortex states and buckle states have been seen in samples of this size by Endean,[1] Youngblood,[2] and the author. It is necessary to differentiate between samples that have a vortex ground state and a buckle ground state since a buckle state has a net magnetization direction that can change direction which we can measure, whereas a vortex state does not. The best way to determine which ground state a particular sample has it to take measurements of hysteresis in the AMR measurements while sweeping the field from a negative value to a positive value and back again with the field being in plane and along the flats of the sample. An example of the hysteresis curves for both a vortex and buckle ground state in two different samples are shown in Fig. 4.1. The difference in the AMR measurement between the two is that the vortex ground state forms abruptly before reaching zero field and becomes destroyed again at higher fields, whereas the buckle state has only one abrupt transition in each field sweep direction associated with magnetic reversal. This reversal in all buckle samples measured occured at about 110 Oe. For a more in depth analysis of this behavior, both Endean and Youngblood described the micromagnetics in their theses.[1,2]

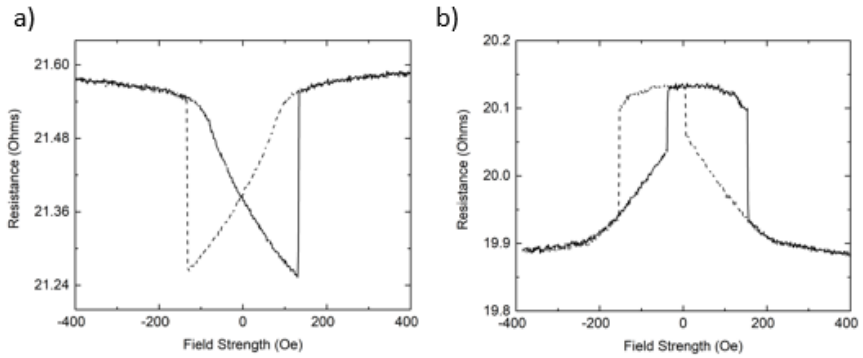

Figure 4.1: Hysteresis measurements of a) buckle ground state and b) vortex ground state in two different samples. The field was applied in the plane and along the flats of the sample. The solid line are the measurements from sweeping the field from the negative to the positive and the dashed lines are from sweeping the field from the positive to the negative.

From LLG Simulations of the samples performed with zero field, the samples should in fact form a vortex state. But if the vortex is destroyed by first applying a saturating field along the diagonal in the simulation, a buckle state is formed when returning to zero field. The difference in energy between these two states is on the order of 20 eV. This suggests that there is some barrier between the two states and that barrier likely depends on manufacturing differences between samples such as edge roughness. If this barrier was reduced to being on the order of thermal energies, it is likely that the sample will reenter a vortex ground state again despite the vortex being initially destroyed by a saturating field.

For the purposes of this experiment, samples that enter a vortex state are not used since the transition to the vortex state in all samples occurs near 60 Oe which is close in magnitude to the field necessary to induce random telegraph noise (RTN) in some samples.

4.1.2 AMR Signal Size

By measuring the Fractional AMR Signal size, which is the ratio of the measured AMR signal size as a function of field strength versus maximum AMR signal size as described

in 3.3.2, for various temperatures, a non-monotonic behavior is seen as shown in Fig. 4.2. As the temperature is increased, the fractional AMR at fields less than 70 Oe decreases. As the field strength is increased from 0 Oe to 70 Oe, the AMR signal size for higher temperatures increases until it becomes equal to the fractional AMR values for lower temperatures. Each curve ends at the field strength at which RTN is observed since it no longer becomes clear what the AMR signal size is with the random fluctuations.

A possible explanation for this dip is that as the temperature increases, the magnetization inside the sample becomes more curved and comes closer to reforming a vortex ground state as described in 4.1.1. This has the result of lowering the fractional AMR size since a vortex has no net magnetization direction and the difference in resistance between the field measured at 0^o and 90^o tends towards zero. As the field strength is increased, the sample's magnetization aligns with the field resulting in the magnetization curving less and further away from being able to form a vortex state. Near 70 Oe, the field is able to overcome this temperature induced curling and the fractional AMR signal is made similar to that measured at 5 K. Additional evidence that the cause is the system being closer to forming a vortex is that the energy difference between the vortex ground state and the buckle ground state obtained from simulations is close to 20 eV as previously mentioned, as is the Zeeman energy from a 70 Oe field applied to a permalloy sample of this size.

From Eq. 3.3, it is possible to find what fraction of the sample volume that is able to switch between the two well directions at zero field by assuming that the well directions are at 0^o and 90^o. This assumption is based on the energy landscape that the system is modeled on using Eq. 2.5 where at zero field, the magnetization can only point along the flats of the square. For the case of these samples, that volume fraction of the sample that participates in the magnetic switching appears to be near 0.7 or 70%. The switching volume fraction with an applied field is not able to be determined since the assumption that the wells are at 0^o and 90^o breaks down. With increasing field, the two wells each move towards 45^o.

4.1.3 Barrier Heights

The barrier heights for each of the wells in each sample were measured using the method outlined in 3.3.1 at two different temperatures: 5 K and room temperature. A graph

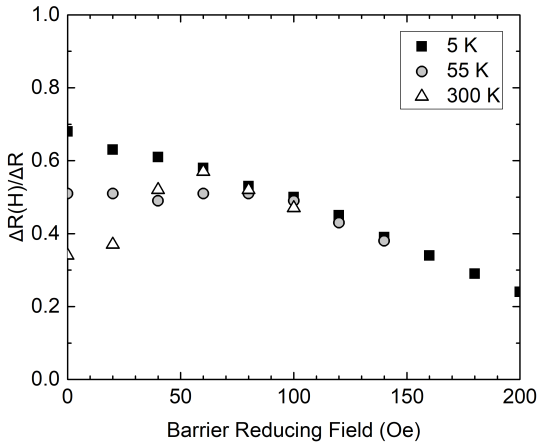

Figure 4.2: Measurements of the Fractional AMR from Eq. 3.3 versus applied field for three temperatures. The 300 K temperature curve is non-monotonic.

showing the distributions of one well's barrier height versus the other well's barrier height for multiple samples is shown in Fig. 4.3. The difference in barrier heights between the two wells of a given sample are more often a sizable fraction of their values, being as high as up to 40%. This can be attributed to manufacturing defects in the samples such as rough edges and slight deviations from a perfect square shape. Since the barrier heights can be different for the two wells, it will have the effect of changing the form of the energy landscape, but Eq. 2.5 is still used as our model of the anisotropy energy. If the barrier heights between the wells are too different, it is necessary to apply the magnetic field at an off-diagonal angle to bring the barrier heights of the two wells closer together. If the barriers were significantly different, while attempting to measure two-state switching, the magnetization would either point towards one well direction for times much longer or much shorter than practically measurable. This restoring of the barrier heights to being closer to each other returns the system close to the model allowing its continued use.

An example of the average barrier height in a sample is shown in Fig. 4.4. Also included are the results for the barrier heights as function of field from the simulations described in 3.4 and barrier heights derived from the RTN data which will be described

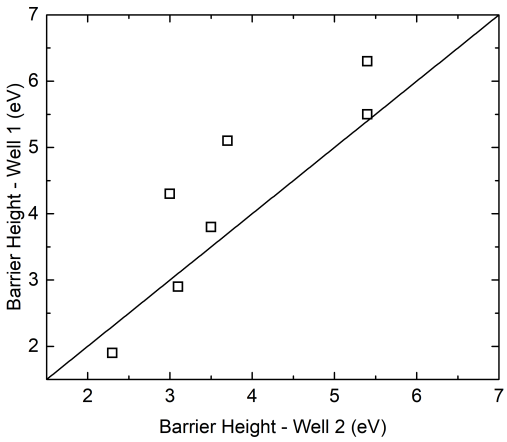

Figure 4.3: Barrier heights of the two wells in a sample versus each other. The solid line is to denote where the points would be if the barrier heights of each well were the same value.

in the next section. To calculate the size of the barriers in zero field, the volume in Eq. 3.1 was decreased to 70% of the total dot volume based on the results of the previous section where the zero field switching volume was found to be 70%.

The result is that the measured barrier heights are approximately 3.2 eV and 2.6 eV at 5 K and room temperature respectively for this sample. These values are consistent with those measured by D. Endean.[1] The difference in the measured values at different temperatures is likely due to larger thermal fluctuations allowing the magnetization to transition over the barrier with a smaller switching field resulting in a smaller measured barrier height at higher temperatures. These measured values are much smaller than the values derived from the simulations and are potentially due to manufacturing defects such as rounded corners lowering the size of the barrier.

A fit of the RTN derived barrier heights using Eq. 2.6 was performed using a U_o value of 3 eV based on the barrier height measured from the switching fields, an initial volume V_o of 70% of the sample volume, and M_s of 800 emu/cm^3. It is seen from the dashed line of Fig. 4.4 that such a fit results in values that are too low for what is measured since the calculated barrier height reaches zero at approximately 90 Oe. This

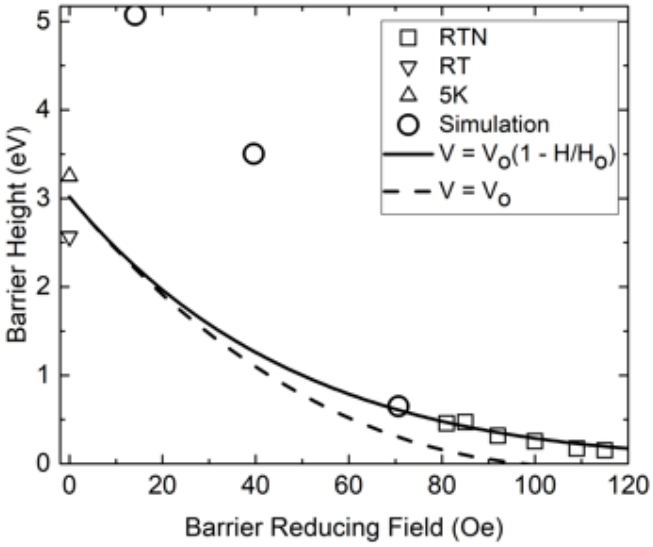

Figure 4.4: Barrier height versus applied field. The triangles are the barrier heights measured using the process in 3.3.1 at both 5K and room temperature. The squares are the barrier heights extrapolated from fits of the RTN data. The circles are the barrier height from simulations as described 3.4. The two lines are fits of the RTN derived barrier heights using Eq. 2.6. The dashed line is for a volume that does not change with applied field strength and the solid line is for a volume that decreases linearly with increasing field strength.

is especially true when taking into account that RTN is seen in some samples at fields of 160 Oe. It is reasonable to believe that a smaller fraction of the volume contributes to the switching behavior in the samples as the field strength is increased. As the field becomes stronger, more and more spins align with it and thus cannot transition between the two states. Approximating this behavior as a linear relationship

$$V = V_o\Big(1 - \frac{H}{H_o}\Big), \tag{4.1}$$

where H_o is a field at which no spins are participating in the switching behavior. Using this linear relationship results in a good agreement between the fit and the data results. By fitting to the data, H_o is determined to be about 250 Oe. This suggests that the volume fraction of the sample's spins that point towards either well decreases with increasing field. Since the field strength directly relates to the size of the barriers where

an increasing field results in a decreasing barrier, it should also be true to say that the switching volume decreases with decreasing barrier height. This makes sense from a picture of just the barrier heights since large barriers mean it is harder for the spins to point towards the barrier direction, a smaller barrier height means more spins are able to point in that direction and require that the switching volume be smaller.

4.2 Characteristic Dwell Times

4.2.1 Dwell Times versus Inverse Temperature

From the time records for over seventy measurements across fourteen samples, an example of which is shown in Fig. 3.4, the dwell time of each transition in each well were calculated as was the average of those dwell times. The distribution of the dwell times on a log scale for each of the two wells of a sample are shown in Fig. 4.5. The dwell times for each well are similar to a log-normal distribution but with a skew towards shorter dwell times which is in contrast with previous work[42–44] which expect an exponential distribution but in agreement with other results[45–47] for nanoscale systems undergoing RTN, in those cases, complementary metal–oxide–semiconductor (CMOS) devices. This skewing towards shorter dwell times suggest that the samples are more likely to switch the shorter amount of time they are in that state which will be explained further in 4.2.4.

The average dwell time in each of the two wells of a sample was plotted versus inverse temperature on a semilog plot as described in 3.3.3. An example of this for both wells in a sample with a single field magnitude and direction is shown in Fig. 4.6. By performing a fit of the data using the log of Eq. 2.24, it is possible to obtain the prefactors from the y-intercept which is an extrapolation to infinite temperature and the barrier height from the slope. As an additional check, we fit a line to all combinations of points from Fig. 4.6 and calculated their slopes and y-intercepts before averaging them together which resulted in similar values for τ_o as the best line fit.

Since we can measure the samples over different temperature ranges and with different applied fields, we are able to get multiple sets of prefactors and barrier heights from the same sample. The multiple prefactors and barrier heights from a single sample can be plotted against each other as shown in Fig. 4.7 where the values in the upper right

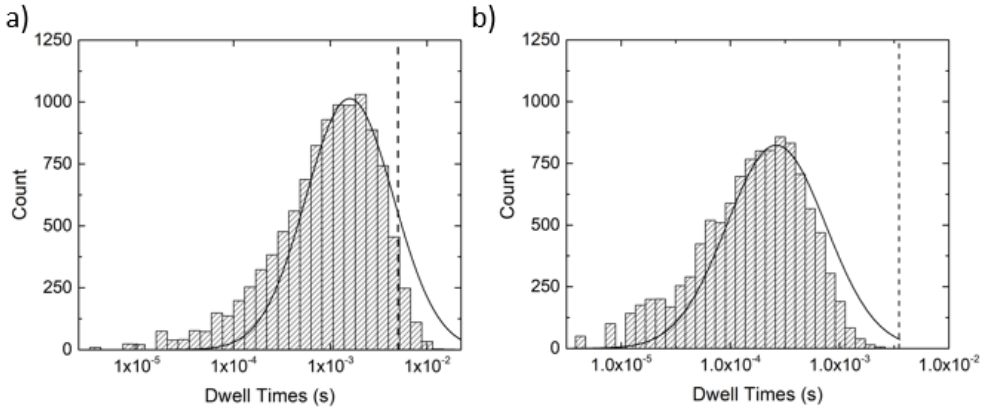

Figure 4.5: Histogram of the dwell times on a log scale for each of the two wells in a sample at a given temperature and field strength. The fitted lines are for a normal distribution on the log scale which shows that the distribution of dwell times follow a log-normal distribution with a skewing towards shorter dwell times. The dashed lines correspond to our assumed thermalization time, τ_{thermal}, which will be discussed in 4.2.4.

are for one well and the values along the bottom are for the other well. This specific example given is from a sample that only required the field strength to be adjusted as the sample warmed instead of also adjusting the angle which was possible in four of the 250 nm samples measured. The prefactors for the two wells are about seven orders of magnitude apart with one well having values near 10^{-6}s and the values for the other well being near 10^{-13}s. It can also be seen that as the barrier heights of each of the two wells increase, the prefactors for each well moves away from the prefactors of the other well. It will be shown that this increasing separation is the result of the prefactors of one well having a dependence on the barrier heights of both wells. This interdependence of the wells will be explained further in 4.2.4.

Prefactor versus barrier height data for six 250 nm samples and eight 210 nm samples are shown in Fig. 4.8. Also plotted is the expected prefactors from Brown's result in Eq. 2.24 at 100 K and an α of 0.01 as appropriate for a thin film of permalloy.[26] For the 250 nm samples in Fig. 4.8a, all the measured prefactors are orders of magnitudes smaller than expected from Eq. 2.24 including prefactors at unphysical time scales of 10^{-15} seconds. Fig. 4.8b has values that range from slightly above the expected prefactors down to much lower values than even the 250 nm samples. Being slightly above the

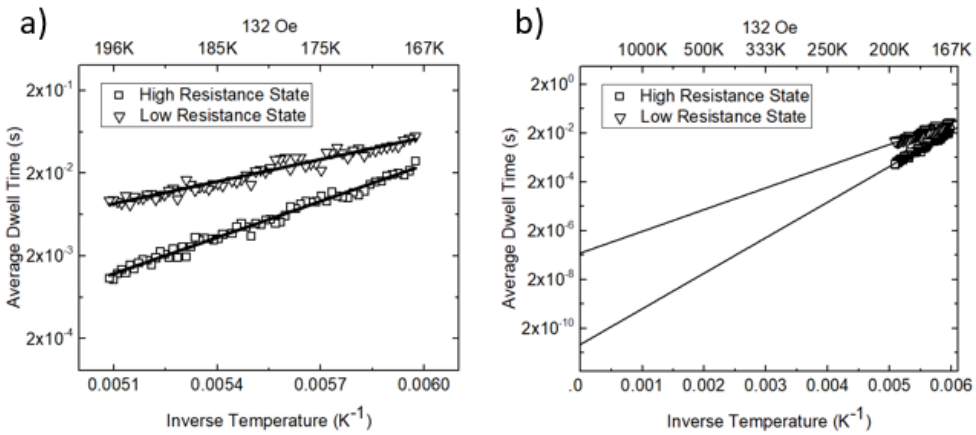

Figure 4.6: a) Average Dwell Times versus Inverse Temperature on a semilog plot for both the high resistance state and the low resistance state in a sample with a 132 Oe applied field. The solid lines are fits done of the data using Eq. 2.24 b) Shows the extrapolation of the fit line to infinite temperature to give the prefactor which is measured as the y-intercept.

expected values is likely due to the extrapolation method for obtaining the y-intercept as described in 4.2.1. Because the temperatures at which the measurements are taken are far away from infinite, the error in the best fit line has been found to be off by as much as an order of magnitude in either direction. This error does not account for the wide display of prefactors over the many orders of magnitude down to 10^{-30}s. For both size samples, there is an overall trend that the largest of the barrier heights has the smallest values of the prefactors. Lastly, the prefactors are orders of magnitude different from those that would be expected from the inverse of the FMR frequency (10^{-10}-10^{-11}s) showing that a common assumption for the value of the characteristic dwell time is not universally correct.

4.2.2 Temperature Dependent Barrier Heights

One possible explanation for others measuring unexpectedly high switching rates was put forth by Stier et al.[48] They suggest that a temperature dependent barrier height can be sufficient to explain the unphysically small prefactors. Since a fit of the data is

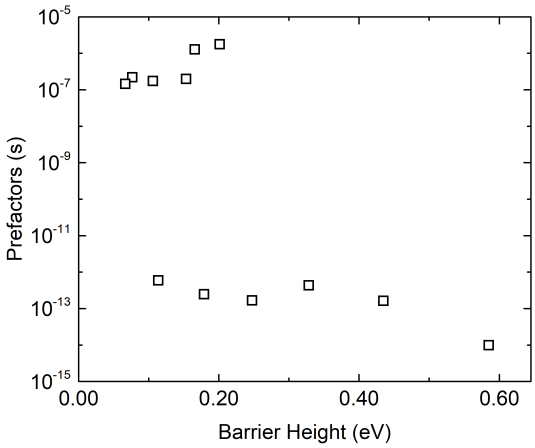

Figure 4.7: Prefactors versus Barrier Height for a single sample. The points in the upper left of the graph are from one well and the points along the bottom of the graph are from the other well.

performed assuming a constant barrier height, a decreasing barrier height with increasing temperature will result in a smaller extrapolated prefactor. Since all values of Eq. 2.24 are known with the exception of the barrier height, it is a simple matter to invert the equation and numerically solve for the barrier height as a function of temperature. Two examples of this being done for different samples is shown in Fig. 4.9. It can be seen that for one sample, the barrier height for both wells decrease with increasing temperature as would be expected from the magnons destroying the magnetization. But for the second sample, the barrier height would in fact have to increase for one of the wells to explain the observed prefactors which is not expected. A barrier height that needs to increase with increasing temperature was seen over different temperatures in this same sample and in two of the other samples as well.

The temperatures at which the samples were measured were less than 300 K which is not near the Curie Temperature, T_C, of permalloy of 850 K. Based on Bloch's Law

$$\frac{M(T)}{M(0)} = 1 - \left(\frac{T}{T_C}\right)^{3/2}, \tag{4.2}$$

there is only an expected drop in the magnetization of 1.3% from 90 K to 110 K and a 1.0% change from 105 K to 120 K which is much smaller than what is required of the

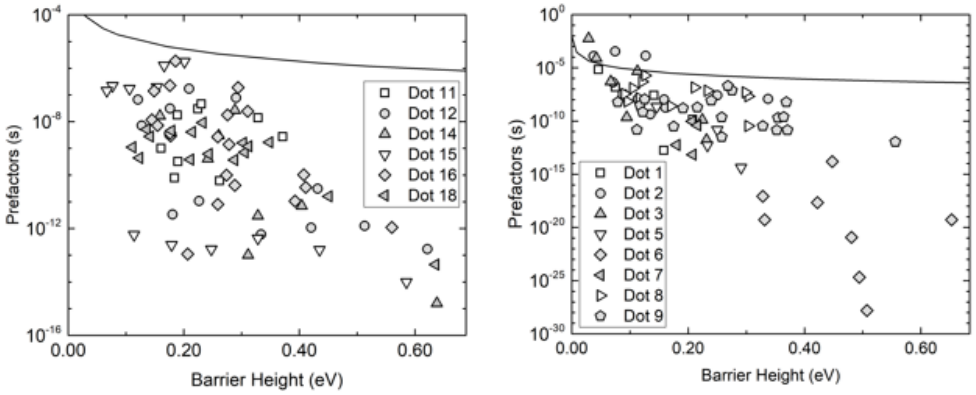

Figure 4.8: Prefactors versus Barrier Heights. Each symbol represents data for one of a) six different 250 nm samples and b) eight different 210 nm samples. The black line is the expected prefactors according to Eq. 2.24 at 100 K. Some sample designations are skipped which is due to those samples breaking before two-state switching could be measured.

barrier height. The much smaller change in magnetization and the increasing barrier height with temperature suggest that a temperature-dependent barrier height is not sufficient to explain the observed characteristic dwell times.

Stier et al. also mention that since the barrier height doesn't exist above the Curie temperature, it would be correct to only extrapolate the fit to that temperature and the fitted value at that point would be the value of the prefactor. But as it can be seen from Fig. 4.6b, even if the fit line was truncated at the Curie temperature of permalloy (850 K), it would only explain about an order of magnitude at most and would be unable to explain obtained values between 10^{-13} and 10^{-30}s.

4.2.3 Detailed Balance

Detailed balance predicts the ratio of the measured dwell times to be given by

$$\frac{\tau_1}{\tau_2} = e^{\frac{(U_1 - U_2)}{k_b T}}, \tag{4.3}$$

based on Eq. 2.40 assuming that τ_o is the same for both wells. As a check of detailed balance, the dwell time from one well at a single temperature was divided by the dwell time from the other well at the same temperature. This was done at each temperature

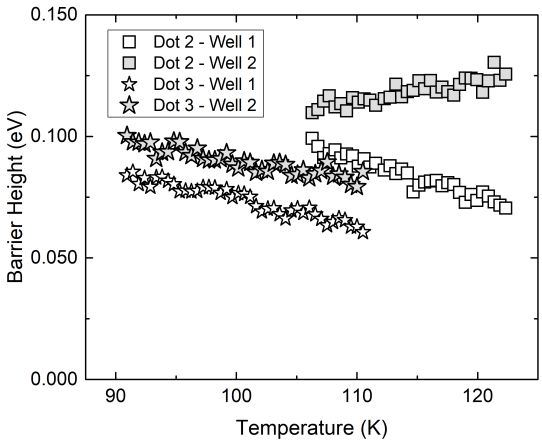

Figure 4.9: Numerically solved barrier heights as a function of temperature for the two wells in two different samples.

for example from the data in Fig. 4.6. These ratios for the data from Fig. 4.6 were plotted versus inverse temperature in Fig. 4.10. These data are linear on a semilog plot where the slope is the difference in barrier heights of the two wells divided by the Boltzmann factor and the extrapolation to infinite temperatures should be equal to unity. As expected, the slope of the line in Fig. 4.10 is equal to the difference in barrier heights of the two curves in Fig. 4.6 divided by the Boltzmann factor. Surprisingly, the extrapolation to infinite temperature was not unity as expected from Eq. 2.40. Instead, the extrapolation gave a value close to 2×10^5.

Detailed balance was checked for all measurements across the fourteen samples and for all cases, we find the y-intercepts at infinite temperature ranged in value from $1-10^{10}$. This is a clear indication that the expression for detailed balance (Eq. 2.40) requires a prefactor, A_{DB}. Including this prefactor gives a detailed balance relation

$$\frac{\tau_1}{\tau_2} = A_{DB} e^{\frac{U_1 - U_2}{k_b T}}. \tag{4.4}$$

The A_{DB} for all the samples are plotted in Fig. 4.11 versus what we will define as the energy factor given by, $(U_2^2 - U_1^2)/U_1 U_2$. We expect A_{DB} to have a dependence upon the energy factor for three reasons. The first is that the only physical properties of the particles that are changing are the well energies and their temperature but A_{DB} had no

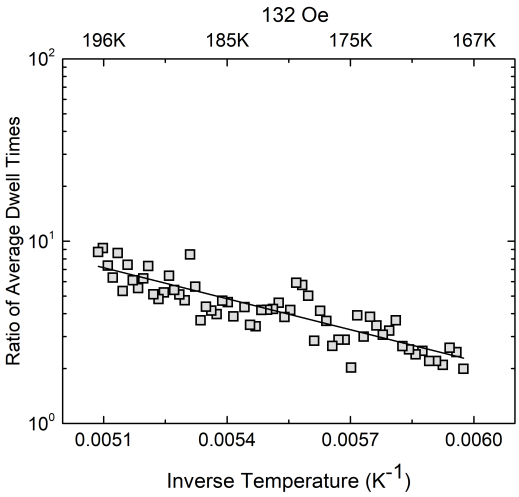

Figure 4.10: Ratio of the average dwell times from Fig. 4.6 versus inverse temperature on a semilog plot. The line is a best fit line of the data where the slope of is equal to the difference of the barrier heights divided by the Boltzmann factor and the y-intercept at infinite temperature should be equal to one based on detailed balance (Eq. 2.40). The prefactor was not unity but close to 2×10^5.

discernable trend with temperature. Second, when the barrier heights are the same size, A_{DB} goes to one which means we are returning to the expected detailed balance of Eq. 2.40. And lastly, we expect this prefactor to be symmetric when exchanging the indices 1 and 2. In addition, since A_{DB} goes to unity as the difference in well heights goes to zero, we expect A_{DB} to have some form of exponential dependence on the energy factor

$$A_{DB} \approx e^{C\frac{U_2^2 - U_1^2}{U_1 U_2}}, \tag{4.5}$$

where C is a fitting parameter. The energy factors for all A_{DB} are positive by our convention of dividing the small well dwell times by the large well dwell times. With this added term, the Arrhenius law, Eq. 2.24, becomes

$$\tau_1 = \tau_o e^{C\frac{U_2}{U_1}} e^{\frac{U_1}{k_b T}}. \tag{4.6}$$

If Eq. 4.6 for both τ_1 and τ_2 are taken in ratio, the ratio will be Eq. 4.4 is recovered with the form of A_{DB} from Eq. 4.5.

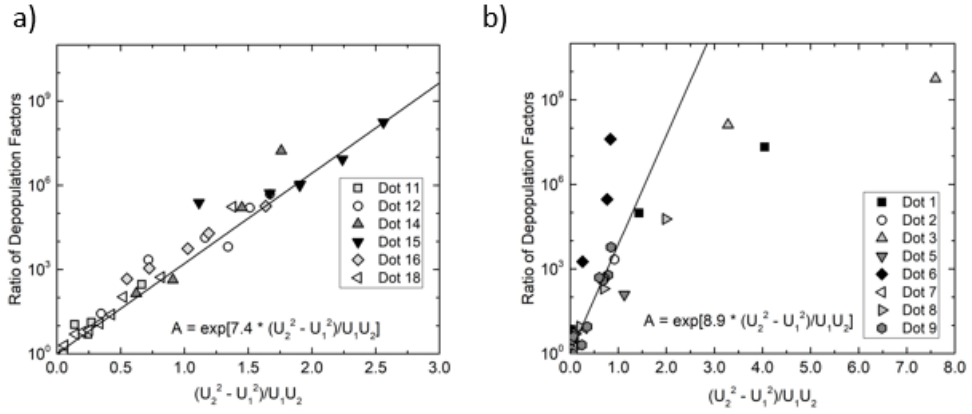

Figure 4.11: Additional prefactor term from Eq. 4.5 plotted as a function of the well energies as described in this section. a) is for samples that are 250 nm on a side and b) are for samples that are 210 nm on a side. The lines are fits to Eq. 4.6 with the constant, C, of 7.4 for the 250 nm particles and it is 8.9 for the 210 nm particles.

As can be seen in Fig. 4.11(b), there are deviations from this simple exponential form for large energy differences between the wells. With the form of A_{DB} in Eq. 4.5, it would only be able to explain the behavior seen at low energy factors as seen in Fig. 4.11 and be unable to explain the deviation seen at higher energy factors. In Fig. 4.8, the measured prefactors are smaller than what is expected according to Brown's result in Eq. 2.24 (indicating shorter characterisitc dwell times or faster transitions). On the other hand, Eq. 4.6 can only have values greater than one for positive values of the fitting constant, C, meaning that Eq. 4.6 can only increase dwell times. A more appropriate form of A_{DB} that explains both the behavior seen in Figs. 4.8 and 4.11 will be presented later in 4.2.4.

Time records from simulations of time dependent, magnetic two-state switching of particles as described in 3.4 were obtained at 300 K, 290 K, and 280 K with applied fields around 60 Oe. The applied fields were taken off diagonal to create uneven wells. From the time records, A_{DB} was calculated for over twenty five different field strengths and directions; the A_{DB} values from simulations are shown in Fig. 4.12. Up to the fitting constant, the results from the simulations replicate the data.

At first glance, the additional prefactor term of Eq. 4.6 would appear to violate

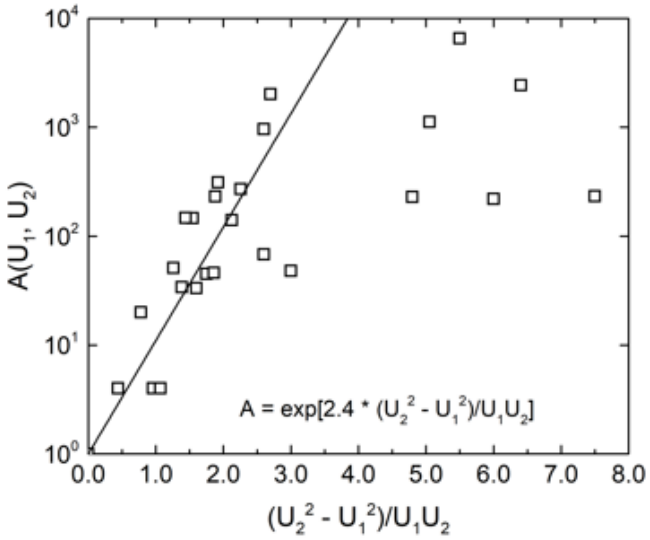

Figure 4.12: Detailed balance prefactors A_{DB} versus the energy factor for simulated, magnetic two-state switching on a semilog plot. The fitted line is the exponential given in the plot performed up to an energy factor of 3.0 before the points start to curve over.

detailed balance but is actually needed to restore the detailed balance in accordance with Eq. 2.40. Because the two wells are almost always uneven, there is an effective internal, magnetic field pointing from the shallow well to the deeper well. In addition, the externally applied magnetic field may not be perfectly aligned with the diagonal which gives a component pointing from one well to the other. Either of these two fields would break time reversal requiring the extra step described in the 2.2.5 section. Reversing the direction of the net magnetic field reverses the energies of the wells such that $U_1 \rightarrow U_2$ and $U_2 \rightarrow U_1$ resulting in the detailed balance equation becoming

$$\frac{\tau_1 e^{C\frac{U_1}{U_2}}}{\left(\tau_2 e^{C\frac{U_2}{U_1}}\right)^*} = \frac{\tau_1 e^{C\frac{U_1}{U_2}}}{\tau_2 e^{C\frac{U_1}{U_2}}} = \frac{\tau_1}{\tau_2} = e^{\frac{U_1 - U_2}{k_b T}}. \tag{4.7}$$

This results in Eq. 2.40 being restored which is our detailed balance requirement.

4.2.4 Multidimensional Solution

When Brown derived his solution in Eq. 2.24, he made two assumptions that we need to address: first, the particle was a single domain macrospin where all the spins are

aligned, and second, the system was in thermal equilibrium before transitioning. His first assumption clearly does not hold in our system as our particles are almost two orders of magnitude larger than the exchange length of permalloy (5.7 nm).[38] This means we must use the multidimensional solution of Eq. 2.32 that accounts for multiple exchange length sized macrospins attempting to clear the barrier individually.

We started with calculating the eigenvalues of the Hessian matrix, K, from Eq. 2.8 using a program that calculates the second derivatives of the energy with respect to each macrospin's polar angle degree of freedom. Using LLG Micromagnetics Simulator as described in 3.4, calculations of the macrospin states (list of the angle cosines for each unit cell's magnetization) were made for the net magnetization pointing toward the energy maximum and when pointing towards a minimum at various applied field strengths for both. We evaluated K at both states and then diagonalized it to get the eigenvalues for both the energy maximum, λ^s, and the minimum state, λ^m. Using only the positive eigenvalues (stable modes), the prefactor for the multidimensional solution was calculated using

$$\tau_o \propto \frac{\Pi_i \lambda_i^s}{\Pi_i \lambda_i^m} \tag{4.8}$$

based on Eq. 2.32 with the results plotted in Fig. 4.13. This figure indicates that τ_o is predicted to decrease with increasing magnetic field but since the increasing magnetic field decreases the barrier height, this prediction is not physical.

To further verify the multidimensional solution doesn't explain our experimental results, we calculated the ratio of the prefactors for double wells in a given field and temperature from Eq. 4.8. To approximate the barrier height, we set the barrier height equal to 3 eV at 0 Oe based on measurements we made using the method described by Endean et al.[9] shown in 4.1.3. We then made a linear approximation such that the barrier height reached 0 eV at 75 Oe based on simulations showing the barrier disappears near 75 Oe. For every combination of points from Fig. 4.13, we then evaluated Eq. 4.8 for the more shallow energy well, τ_L, and for the more deep energy well, τ_H, and using the approximated barriers from the linear energy approximation. The ratio of τ_L and τ_H is

$$\frac{\tau_L}{\tau_H} \propto (\frac{\Pi_i \lambda_i^s}{\Pi_i \lambda_i^m})_L / \frac{\Pi_i \lambda_i^s}{\Pi_i \lambda_i^m})_H = (\frac{\Pi_i \lambda_i^s}{\Pi_i \lambda_i^m})_L (\frac{Pi_i \lambda_i^m}{\Pi_i \lambda_i^s})_H. \tag{4.9}$$

Assuming the product of the eigenvalues for the saddle point, or energy maximum, are

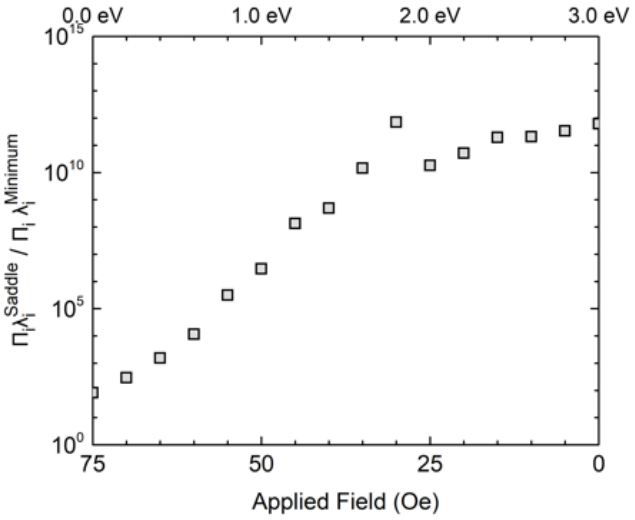

Figure 4.13: A plot of the ratio of products of eigenvalues from Eq. 4.8 versus applied field on a semilog plot using simulation data. As applied field increases to the left, that is equivalent to saying the barrier height is increasing to the right which is shown on the top axis where the field is assumed to decrease from 3 eV to 0 eV from 0 Oe to 75 Oe.

the same for both wells, this ratio reduces to

$$\frac{\tau_L}{\tau_H} \propto \frac{(\Pi_i \lambda_i^m)_H}{(\Pi_i \lambda_i^m)_L}. \tag{4.10}$$

The result for Eq. 4.10 is plotted in Fig. 4.14 where each line represents keeping $(\Pi_i \lambda_i^m)_H$ constant and allowing $(\Pi_i \lambda_i^m)_L$ to vary. The results decrease over many orders of magnitude at lower values of the energy factors and level out at high energy factors.

The multidimensional prefactors from Eq. 4.8 have the opposite trend of the experimentally measure values (Fig. 4.8) when compared to the barrier heights, similarly, Fig. 4.14 has the opposite trend of what we see experimentally from the ratio of prefactors as shown in Fig. 4.11. Equation 4.8 can only lead to larger prefactors with increasing barrier height when we see smaller prefactors with larger barrier heights. Equation 4.10 can only lead to a smaller ratio of the average dwell times while what is observed is an increasing ratio of the average dwell times.

It is important to note in all the modelling of Brown and Kramers discussed so far, they assumed the system returns to thermal equilibrium before transitioning.[5,13,14,18,22]

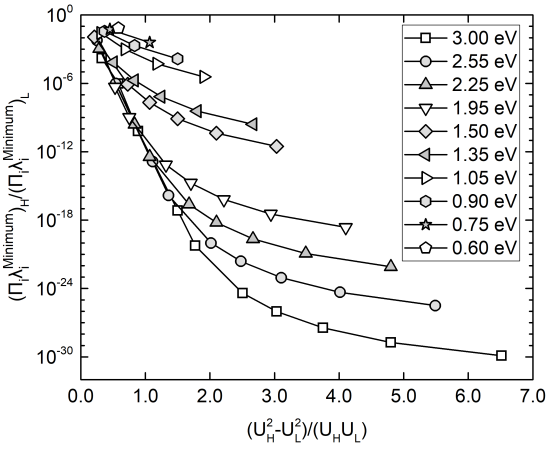

Figure 4.14: Ratio of the higher barrier height well's product of minimum eigenvalues over the lower barrier height well's product of minimum eigenvalues from Eq. 4.10 versus the energy factor on a semilog plot. Each line represents keeping $(\Pi_i\lambda_i^m)_H$ constant and allowing $(\Pi_i\lambda_i^m)_L$ to vary where the constant value is associated with the well of the height listed in the key.

This assumption means that the particles in the well will spend most of their time at the well minimum in a Boltzmann distribution of states (thermal equilibrium). Of course when a particle transitions over the barrier it has excess energy, they are assuming it is rapidly lost i.e. τ_{thermal}, is much shorter than the dwell time. On the other hand, if the system transitions at times much faster than τ_{thermal}, then a different model is required. This is the approach taken by Talkner's derivation of transition rates for a system far from thermal equilibrium due to being in the VLD regime as shown in Eq. 2.36.

Talkner suggests that the switching time is inversely proportional to the probability of the system being near the saddle point compared to near the bottom of the well. For a system out of thermal equilibrium, this ratio can be much less than unity due to the system having excess energy from each transition, allowing it to exist near the saddle point for longer periods of time. As a check to see if our system could be transitioning before reaching thermal equilibrium, we look back to Eq. 2.31. Assuming that Brown's derivation can give us an approximate indication for the time of each oscillation, our system has $\tau_o \approx 5 \times 10^{-5}$ s which is calculated from Eq. 2.24 at 300 K and $\alpha = 0.01$.[26]

This assumption gives a τ_{thermal} that is approximately 5×10^{-3} s. If an appreciable number of transitions are on this scale and faster, then the system is transitioning before reaching equilibrium. This is in contrast with nanoparticles which have a τ_o on the order of 10^{-9} s based on Eq. 2.24 which would hide this effect when transitions are measured on typical laboratory time scales ($10^{-3} - 10^{0}$ s).[21]

Histograms for the dwell times at a fixed temperature and field for two typical samples are shown in Fig. 4.5. Many of the transitions occur well below 5×10^{-3} s, meaning that they are switching before our assumed τ_{thermal} which implies the possibility of our system transitioning before reaching thermal equilibrium. A normal fit of the logarithmic distributions of dwell times is also shown in Fig. 4.5 which shows that the dwell times are skewed towards having more transitions at shorter dwell times. This suggests that the system has a higher probability to transition the less time the system is in that state because the system will have more of its excess energy from the previous transition. This leads us back to Talkner's results for a system that is spending most of its time near the saddle point instead of well minimum.[31]

Since our system is potentially out of thermal equilibrium, we evaluate Eq. 4.8 with that in mind. When we evaluate the eigenvalues of the Hessian matrix from Eq. 2.8, our degrees of freedom are the macrospin's polar angles. This means that the eigenvalues maintain units of energy and are the amount of energy necessary to excite their corresponding normal mode. When the system transitions over the barrier from one well into another, the system has the energy equivalent to the height of the barrier of the well it transitions into. This means we only include in Eq. 4.8, the eigenvalues that have energy smaller than the barrier height. The barrier height of the well is inversely proportional to the magnitude of the applied field, so as the applied field is increased the number of modes that are accessible to the system will decrease. Using the same linear relationship between the barrier height and applied field magnitude we used to approximate the barrier height in Fig. 4.13, the results for Eq. 4.8 are shown in Fig. 4.15. Based on the number of unit cells we used, we obtained 2,500 eigenvalues that ranged in value from -300 meV to 5500 meV. For the data points in Fig. 4.15, our cutoff energies ranged from 200 meV to 1000 meV.

Using Talkner's result and the energy restriction, we see that the prefactors decrease with increasing barrier height as seen in Fig. 4.15. This is in accordance with what we

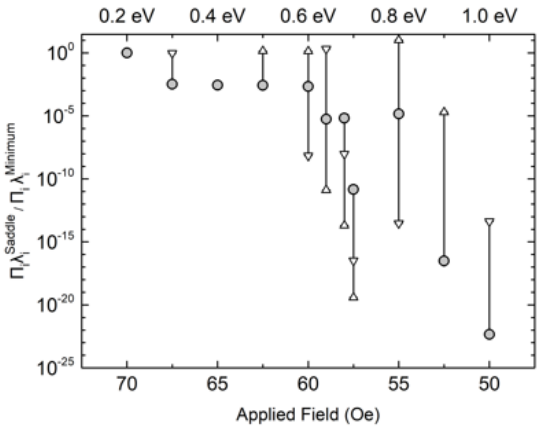

Figure 4.15: A plot of the ratio of products of eigenvalues from Eq. 4.8 versus applied field on a semilog plot using simulation data where all the eigenvalues have energies smaller than the barrier height at that field. As applied field increases, that is equivalent to saying the barrier height is decreasing. The error bars are for assuming the eigenvalue's cutoff energy can be ±5% from our assumed barrier height energy. For example, if the cutoff energy is 500 meV, we evaluated Eq. 4.8 for energies less than 475 meV, 500 meV, and 525 meV. The right-side-up triangle represents the 5% larger cutoff energies and the upside-down triangles represent the 5% smaller cutoff energies.

see experimentally (see Fig. 4.8). Next, we check to see if this solution also satisfies the results we see for the ratio of prefactors in Fig. 4.11. By taking the ratio of each point in Fig. 4.15 with each other point using Eq. 4.10, and plotting them compared to that ratio's energy factor, we obtain curves that behave similarly to Fig. 4.11 as seen in Fig. 4.16. The lines connect points where the numerator in Eq. 4.10 is kept constant and the denominator is allowed to change. This gives the behavior if one well depth is kept constant and the other is allowed to get larger. This similar trend for both Fig. 4.15 and Fig. 4.16 to our experimental data suggests that the system is spending most of its time out of thermal equilibrium which means it stays closer to the saddle point increasing the probability of transitions and thus increasing the transition rate.

This argument, along with the internal field discussed in 4.2.3, can also be used to explain the increasing separation of the prefactors with increasing difference in barrier heights seen in Fig. 4.7. As the barrier height difference becomes larger between the two wells, the internal field pointing from the shallow well to the deeper well gets larger.

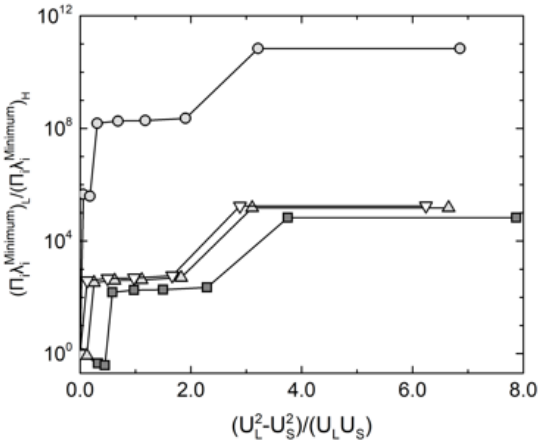

Figure 4.16: Ratio of the higher barrier height well's product of minimum eigenvalues over the lower barrier height well's product of minimum eigenvalues from Eq. 4.10 versus the energy factor on a semilog plot where all the eigenvalues have energies smaller than the barrier height.

As the magnetization moves to the deeper well, the field gives it more excess energy allowing it to transition back faster. But when the magnetization is moving against the field, it loses some of that energy resulting in it spending more time in the shallow well than it would without the field.

So to reiterate, the particles transition back to the previous well before the system can reach equilibrium, or a Boltzmann energy distribution. This is consistent with our data and possibly due to our system being in the very low damping regime where the system is less able to dissipate energy to the heat bath. This leads to different dynamics in our system that is explained by Talkner where our results can be explained by assuming that our system is spending much of its time near the saddle point relative to the well minimum which drastically decreases our measured prefactors from Brown's result.

Chapter 5

Conclusion and Future Work

5.1 Conclusion

Previous theories that require the system return to thermal equilibrium after transitioning over the barrier prior to being able to transition again have proven inadequate to describe the two-state switching behavior we see in square, mesoscale permalloy particles. The dwell time between switching events required prefactors of the Arrhenius law that were smaller by up to twenty orders of magnitude than the expected prefactors proposed by previous theories with the results shown in Fig. 4.8. These prefactors with an unphysical timescale are what motivated this investigation since switching was seen faster than any relevant rate such as the FMR frequency. In addition, when attempting to analyze the detailed balance of the system using ratios of the measured prefactors, an extra term depended on the wells' relative energies was needed to explain the data; these ratios are presented in Fig. 4.11. These two behaviors led us to the work of Talkner who derived the transition rate for a system that depends on the relative time the system spends near the saddle point compared to the well minimum.

Talkner's model suggests that the dwell time is inversely proportional to the likelihood of finding the system near the saddle point compared to the well minimum. We expect that the magnetization is switching before reaching thermal equilibrium which would result in the system spending more time near the saddle point than near the well minimum, speeding up the transition rate. This would occur if the time it takes to thermalize the system (return to a Boltzmann distribution of states), τ_{thermal}, is larger than

the average dwell time, τ. For the system to be out of thermal equilibrium, it means that the system has not lost the excess energy from the previous transition which allows it to transition back over the barrier earlier than if it had to wait to reach equilibrium.

His model states that the dwell time

$$\tau = \tau_o \frac{\Pi_i \lambda_i^s}{\Pi_i \lambda_i^m} e^{\frac{U}{k_b T}}, \tag{5.1}$$

depends on τ_o which is the time it takes for the system to move away from the saddle point, $\Pi_i \lambda_i^s$ and $\Pi_i \lambda_i^m$ which are the products of the eigenvalues of the Hessian matrix and are inversely proportional to the likelihood of finding the system near the saddle point and well minimum respectively, and the Boltzmann factor. For our analysis, we capped the eigenvalues used in the products to only those eigenvalues whose energy is smaller than the height of the barrier. This yielded results that showed similar trends as our experimental results and are shown in Fig. 5.1. For Fig. 5.1, we set τ_o from Eq. 5.1 to be equal to 5×10^{-5} s based on Brown's result in Eq. 2.24 and for ease of comparison between the simulation results to experimental.

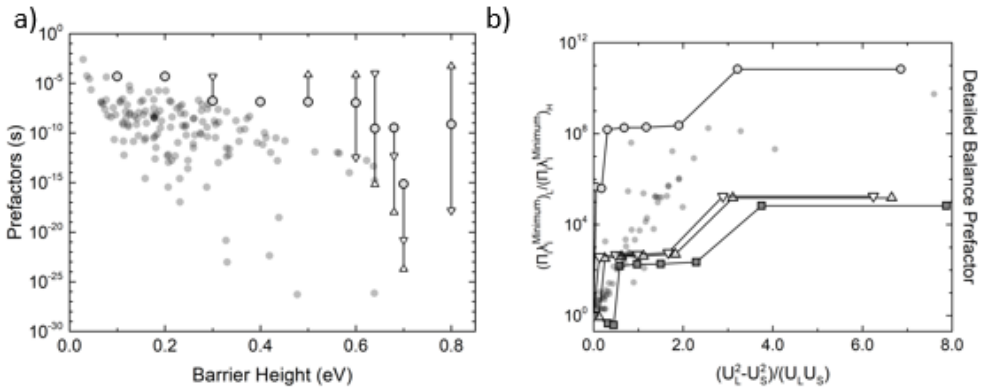

Figure 5.1: Experimental results for both a) measured prefactors (Fig. 4.8) and for b) the ratio of the prefactors (Fig. 4.11) compared to simulated results (Figs. 4.15 and 4.16 using Talkner's derivation in Eq. 5.1.

5.2 Future Work

If the problem is in fact that we are transitioning before reaching thermal equilibrium, it should be possible to check by measuring on time scales where the average dwell time is much larger than the thermalization time, τ_{thermal}. Based on a τ_{thermal} of 5×10^{-3} such as we approximate for our system and the three orders of magnitude spread we see in our distribution of dwell times in Fig. 4.5, we would need to measure average dwell times of greater than 10 s over a range of temperatures. This would require precise temperature control of the cryostat system to sit at a temperature for an hour or more to collect a sufficient number of measured transitions to ensure a proper average of dwell times at each temperature. Since this would require our closed cycle system to be running while sampling data, extra noise considerations would need to be taken to ensure a proper signal is seen.

To measure two-state switching of the proper timescales, it is necessary to have a map of the temperatures and barrier heights that give a sufficient amount of time for the system to thermalize. Equation 5.2 incorporates how we need to see average dwell times greater than 10 seconds based on being four orders of magnitude longer than τ_{thermal}. We also assume that the prefactors in Fig. 4.8 follow a simple exponential relation with respect to the barrier height. The result of these two assumptions gives

$$\tau > 10^4 \times \tau_{\text{thermal}} > 10s = 10^{-5} s e^{\frac{U}{333K}} e^{\frac{U}{k_b T}}. \tag{5.2}$$

When Eq. 5.2 is solved for the barrier height as a function of temperature, the result is

$$U = \frac{-(13816K)k_b T}{3T - 1000K}, \tag{5.3}$$

which is plotted in Fig. 5.2. The plot shows the line that gives the division between dwell times that are less than and greater than 10 s. By being above the line, we would expect the system to be in thermal equilibrium if our assumed τ_{thermal} is correct. Also plotted are an assortment of the average temperature and barrier heights that were measured for this report which shows that the data we took was well within the range of what we assume to be not in equilibrium. As data is taken above and further from the line, we would expect to see some form of transition in the prefactor from Eq. 4.8 to no longer decrease with increasing barrier heights.

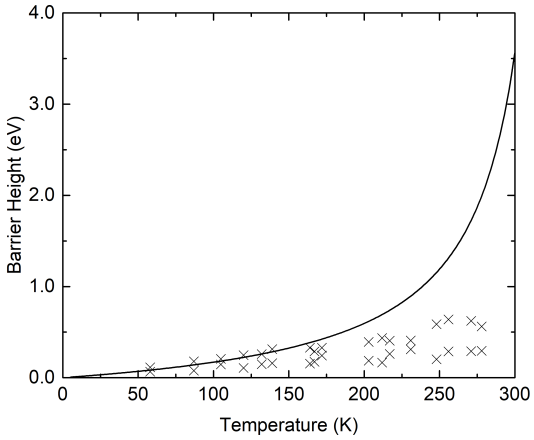

Figure 5.2: The separating line between transitions that occur before reaching thermal equilibrium and after on a plot of barrier height versus temperature. The line is Eq. 5.3 and the crosses are where an assortment of the data taken for this report were taken.

References

[1] Daniel E Endean. *The origin of magnetic noise in nanoscale square dots*. PhD thesis, University of Minnesota, 2014.

[2] Bern Youngblood. *Two-level noise and stochastic resonance in individual permalloy nanoscale magnets*. PhD thesis, University of Minnesota, 2015.

[3] Barry Costanzi. *Emergent 1/f noise in systems of oscillating nanomagnetic dots*. PhD thesis, University of Minnesota, 2016.

[4] Barry N Costanzi and E Dan Dahlberg. Emergent 1/f noise in ensembles of random telegraph noise oscillators. *Physical review letters*, 119(9):097201, 2017.

[5] William Fuller Brown Jr. Thermal fluctuations of a single-domain particle. *Physical Review*, 130(5):1677, 1963.

[6] RI Joseph and E Schlömann. Demagnetizing field in nonellipsoidal bodies. *Journal of Applied Physics*, 36(5):1579–1593, 1965.

[7] RP Cowburn, AO Adeyeye, and ME Welland. Configurational anisotropy in nanomagnets. *Physical review letters*, 81(24):5414, 1998.

[8] Russell P Cowburn and Mark E Welland. Phase transitions in planar magnetic nanostructures. *Applied physics letters*, 72(16):2041–2043, 1998.

[9] Daniel E Endean, CT Weigelt, RH Victora, and E Dan Dahlberg. Measurements of configurational anisotropy in isolated sub-micron square permalloy dots. *Applied Physics Letters*, 103(4):042409, 2013.

[10] RH Victora. Predicted time dependence of the switching field for magnetic materials. *Physical review letters*, 63(4):457, 1989.

[11] S Arrhenius. A method for polarizing more number of impurity-vacancy dipoles. *Zeitschrift für Physikalische Chemie*, 4(226), 1889.

[12] Henry Eyring. The activated complex in chemical reactions. *The Journal of Chemical Physics*, 3(2):107–115, 1935.

[13] Hendrik Anthony Kramers. Brownian motion in a field of force and the diffusion model of chemical reactions. *Physica*, 7(4):284–304, 1940.

[14] Peter Hänggi, Peter Talkner, and Michal Borkovec. Reaction-rate theory: fifty years after kramers. *Reviews of modern physics*, 62(2):251, 1990.

[15] Ralph Skomski, Roger D Kirby, and David J Sellmyer. Activation entropy, activation energy, and magnetic viscosity. *Journal of applied physics*, 85(8):5069–5071, 1999.

[16] LD Landau and EM Lifshitz. On the theory of the dispersion of magnetic permeability in ferromagnetic bodies, phy. z. sowjetunion 8: 153 (1935). *Reproduced in Collected Papers of LD Landau*, pages 101–114.

[17] Thomas L Gilbert. A phenomenological theory of damping in ferromagnetic materials. *IEEE Transactions on Magnetics*, 40(6):3443–3449, 2004.

[18] William T Coffey and Yuri P Kalmykov. Thermal fluctuations of magnetic nanoparticles: Fifty years after brown. *Journal of Applied Physics*, 112(12):121301, 2012.

[19] Neil Smith. Modeling of thermal magnetization fluctuations in thin-film magnetic devices. *Journal of Applied Physics*, 90(11):5768–5773, 2001.

[20] Neil Smith and Patrick Arnett. Thermal magnetization noise in spin valves. *IEEE transactions on magnetics*, 38(1):32–37, 2002.

[21] S Krause, G Herzog, T Stapelfeldt, L Berbil-Bautista, M Bode, EY Vedmedenko, and R Wiesendanger. Magnetization reversal of nanoscale islands: How size and shape affect the arrhenius prefactor. *Physical review letters*, 103(12):127202, 2009.

[22] VI Mel'nikov and SV Meshkov. Theory of activated rate processes: Exact solution of the kramers problem. *The Journal of chemical physics*, 85(2):1018–1027, 1986.

[23] Ivo Klik and Leon Gunther. First-passage-time approach to overbarrier relaxation of magnetization. *Journal of Statistical Physics*, 60(3-4):473–484, 1990.

[24] Yuri P Kalmykov, William T Coffey, Bachir Ouari, and Sergey V Titov. Damping dependence of the magnetization relaxation time of single-domain ferromagnetic particles. *Journal of magnetism and magnetic materials*, 292:372–384, 2005.

[25] Mikihiko Oogane, Takeshi Wakitani, Satoshi Yakata, Resul Yilgin, Yasuo Ando, Akimasa Sakuma, and Terunobu Miyazaki. Magnetic damping in ferromagnetic thin films. *Japanese journal of applied physics*, 45(5R):3889, 2006.

[26] Yaroslav Tserkovnyak, Arne Brataas, and Gerrit EW Bauer. Enhanced gilbert damping in thin ferromagnetic films. *Physical review letters*, 88(11):117601, 2002.

[27] George H Vineyard. Frequency factors and isotope effects in solid state rate processes. *Journal of Physics and Chemistry of Solids*, 3(1-2):121–127, 1957.

[28] Michal Borkovec, John E Straub, and Bruce J Berne. The influence of intramolecular vibrational relaxation on the pressure dependence of unimolecular rate constants. *The Journal of chemical physics*, 85(1):146–149, 1986.

[29] HC Brinkman. Brownian motion in a field of force and the diffusion theory of chemical reactions. ii. *Physica*, 22(1-5):149–155, 1956.

[30] Peter Talkner. Interrelations of different methods for the determination of rates: Flux over population, generalized reactive flux, the lowest eigenvalue and its rayleigh quotient. *Berichte der Bunsengesellschaft für physikalische Chemie*, 95(3):327–330, 1991.

[31] P Talkner. Mean first passage time and the lifetime of a metastable state. *Zeitschrift für Physik B Condensed Matter*, 68(2-3):201–207, 1987.

[32] R.C. Tolman. *The Principles of Statistical Mechanics*. Oxford University Press, 1938.

[33] Sybren Ruurds De Groot and Peter Mazur. *Non-equilibrium thermodynamics*. Courier Corporation, 2013.

[34] M Respaud, M Goiran, JM Broto, F Lionti, L Thomas, B Barbara, T Ould Ely, C Amiens, and B Chaudret. Dynamical properties of non-interacting co nanoparticles. *EPL (Europhysics Letters)*, 47(1):122, 1999.

[35] William Thomson. Xix. on the electro-dynamic qualities of metals:—effects of magnetization on the electric conductivity of nickel and of iron. *Proceedings of the Royal Society of London*, 8:546–550, 1857.

[36] T McGuire and RL Potter. Anisotropic magnetoresistance in ferromagnetic 3d alloys. *IEEE Transactions on Magnetics*, 11(4):1018–1038, 1975.

[37] William H Meiklejohn and Charles P Bean. New magnetic anisotropy. *Physical review*, 102(5):1413, 1956.

[38] R. O'Handley. *Modern magnetic materials*. Wiley-Interscience, 2000.

[39] Harry Nyquist. Certain topics in telegraph transmission theory. *Transactions of the American Institute of Electrical Engineers*, 47(2):617–644, 1928.

[40] Michael R Scheinfein and Elizabeth A Price. Llg user manual v2. 50. *Code of the LLG simulator can be found at http://llgmicro. home. mindspring. com*, 1997.

[41] Arne Vansteenkiste, Jonathan Leliaert, Mykola Dvornik, Mathias Helsen, Felipe Garcia-Sanchez, and Bartel Van Waeyenberge. The design and verification of mumax3. *AIP advances*, 4(10):107133, 2014.

[42] Koichi Fukuda, Yuui Shimizu, Kazumi Amemiya, Masahiro Kamoshida, and Chenming Hu. Random telegraph noise in flash memories-model and technology scaling. In *2007 IEEE International Electron Devices Meeting*, pages 169–172. IEEE, 2007.

[43] Salvatore M Amoroso, Christian Monzio Compagnoni, Andrea Ghetti, Louis Gerrer, Alessandro S Spinelli, Andrea L Lacaita, and Asen Asenov. Investigation of the rtn distribution of nanoscale mos devices from subthreshold to on-state. *IEEE Electron Device Letters*, 34(5):683–685, 2013.

[44] K Takeuchi, T Nagumo, S Yokogawa, K Imai, and Y Hayashi. Single-charge-based modeling of transistor characteristics fluctuations based on statistical measurement of rtn amplitude. In *2009 Symposium on VLSI Technology*, pages 54–55. IEEE, 2009.

[45] Naoki Tega, Hiroshi Miki, Zhibin Ren, PD Christoper, Yu Zhu, David J Frank, Michael A Guillorn, Dae-Gyu Park, Wilfried Haensch, and Kazuyoshi Torii. Impact of hk/mg stacks and future device scaling on rtn. In *2011 International Reliability Physics Symposium*, pages 6A–5. IEEE, 2011.

[46] Simeon Realov and Kenneth L Shepard. Analysis of random telegraph noise in 45-nm cmos using on-chip characterization system. *IEEE Transactions on Electron Devices*, 60(5):1716–1722, 2013.

[47] Zexuan Zhang, Shaofeng Guo, Xiaobo Jiang, Runsheng Wang, Ru Huang, and Jibin Zou. Investigation on the amplitude distribution of random telegraph noise (rtn) in nanoscale mos devices. In *2016 IEEE International Nanoelectronics Conference (INEC)*, pages 1–2. IEEE, 2016.

[48] Martin Stier, Alexander Neumann, André Philippi-Kobs, Hans Peter Oepen, and Michael Thorwart. Implications of a temperature-dependent magnetic anisotropy for superparamagnetic switching. *Journal of Magnetism and Magnetic Materials*, 447:96–100, 2018.

Appendix A

Abbreviations

Acronym	Meaning
AC	Alternating current
AMR	Anisotropic magnetoresistance
CMOS	Complementary metal–oxide–semiconductor
DC	Direct current
FMR	Ferromagnetic resonance
IHD	Intermediate to high damping
IPA	Isopropynol Alcohol
LLG	Landau-Lifshitz-Gilbert
MIBK	Methyl isobutyl ketone
MNC	Minnesota Nano Center
NMP	N-methyl-2-pyrrolidone
PMGI	Polydimethylglutarimide
PMMA	Polymethylmethylacrylate
RTN	Random telegraph noise
UV	Ultraviolet
VLD	Very low damping